# Density-functional theory based calculations of spin-orbit interaction in ZnO



KANAZAWA UNIVERSITY

DISSERTATION

# Density-functional theory based calculations of spin-orbit interaction in ZnO


*Author:*
Moh. Adhib Ulil Absor
1223102008

*Supervisor:*
Prof. Mineo Saito


*A Dissertation submitted in fulfilment of the requirements for the degree of Doctor of Science (D.Sc)*

*in the*

Graduate School of Natural Science and Technology
Kanazawa University

September 2015

List of publications:

1. **Moh. Adhib Ulil Absor**, Hiroki Kotaka, Fumiyuki Ishii, and Mineo Saito, *Tunable Rashba Effect on Strained ZnO: First-principles density-functional study*, Applied Physics Express Vol **7**, pp. 053002 (2014).

2. **Moh. Adhib Ulil Absor**, Fumiyuki Ishii, Hiroki Kotaka, and Mineo Saito, *Persistent spin helix on ZnO* $(10\bar{1}0)$ *surface: first-principles density functional study*, Applied Physics Express Vol **8**, pp. 073006 (2015).

KANAZAWA UNIVERSITY

# *Abstract*

Graduate School of Natural Science and Technology

Division Mathematical and Physical Science

Doctor of Science

by Moh. Adhib Ulil Absor

Recently, the field of spintronics attracted much attention because of their potential application in future electronic devices. The new scheme of spintronics utilizing the effect of spin-orbit interaction (SOI) on the spin textures has been extensively studied. Here, two dimensional electron gas (2DEG) system is an ideal platform because it can be controlled by applying an external electric field or by introducing strain. Wurtzite ZnO is promising materials candidate for spintronics since the high quality of the 2DEG system has been experimentally observed. Therefore, it is crucially important to clarify the effect of SOI in this material, which is expected to induce useful properties for spintronics applications.

In this dissertation, the effect of SOI is studied by using first-principles density-functional theory (DFT). We calculate the spin textures to identify physical properties induced by the SOI. Here, we investigate two different systems, which are (i) the bulk system, and (ii) the surface system oriented on the $[10\bar{1}0]$ direction.

In the case of bulk system, we find that strain controls SOI, where the inversion Rashba rotations are identified. We revealed that the spin-orbit strength can be effectively controlled by tuning the strain. On the other hand, in the case of the surface system oriented to the $[10\bar{1}0]$ direction, we in the first time find that the SOI leads to the novel system called as the persistent spin helix (PSH), exhibiting a quasi-one dimensional orientation of the spin textures. We find that the wavelength of this PSH is smaller than that observed on various zinc-blende quantum well structures.

Finally, we conclude that both the strained bulk and the surface systems are promising for spintronics applications.

# *Acknowledgements*

On this page, I wish to express my sincere gratitude to my supervisors, Prof. Mineo Saito and Prof. Fumiyuki Ishii, for their motivation, support and guidance during my study. They have given me an opportunity and complete freedom to work on interesting research topics during the last three years. This thesis is a result of their consistent encouragement and the fruitful discussions I had with them.

I am thankful to the Directorate General of Higher Education (DIKTI), Indonesia, and Kanazawa University, Japan, for financial support through the Joint Scholarship Program.

I give thanks to all of computational science research group members, especially for Dr. Hiroki Kotaka who teachs me about practical computational based-density-functional theory (DFT) calculations used in this dissertation. I also would like to thank to my Indonesia friends, especially in Indonesia Student Association Ishikawa (PPI Ishikawa) who are always strengthen and supports me in all conditions.

Finally, special thanks to my wife (Fathah Dian Sari) and my children (Alifiah Asma salsabila and Itsna Mutiara Hanifah) for supporting me during my study.

# Contents

# List of Figures

# List of Tables

# Chapter 1

# Introduction

## 1.1 Motivation

Recently, the field of spintronics attracted much scientific interest because of their potential applications in future electronic devices [1, 2]. The spintronics or spin electronics refers to the study of the physical properties of electron spin in solid state physics including generation, manipulation, and detection, and also related to the possible devices by exploiting spin in addition to charge degree of freedom. For example, spin relaxation and spin transport in various metals and semiconductors, which recently attracted much attention in both fundamental research and applications [1], are one of the important issues in the spintronics.

The spin, which is the central object in spintronics, was firstly proposed by Pauli in 1925 [3]. As an additional degree of freedom of elementary particles, its nature has been firstly observed by using the Stern-Gerlach experiment [4, 5]. By using the concepts of spin, Fermions with half integer spin can be distinguished from Bosons with integer spin. Therefore, spin plays an important role in determining the basic concepts of the statistics of the elementary particles. The properties of the electron spin can be observed in the systems which rely on magnetism. Here, ferromagnetic materials [6–8], which is recently used in the various electronic devices, is one of the example system showing the appearence of spin in materials.

One of the most important discovery of spintronics is giant magnetoresistance (GMR), which was observed in metallic multilayers by using a spin-dependent electron transport measurement [9, 10]. Recently, the GMR effect has already

been used practically in the hard disk drive heads. The discovery of GMR was preceded by the observation of the tunnelling magnetoresistance (TMR) [11–15], which has been realized on the magnetoresistive random-access memory (MRAM) devices. Furthermore, the next generation of the spintronics has been focused on the semiconductor class, such as dilute magnetic semiconductors (DMS), which has been extensively studied [16, 17]. Here, some of new physical properties which is useful for spintronics such as carrier-induced ferromagnetism [18, 19] and photoinduced ferromagnetism were found [20–23].

Thus far, recent development of spintronics relies on the new pathway for exploiting carrier spins in semiconductors without any addition of magnetic materials or external magnetic fields, which can be realized by utilizing the effect of spin orbit interactions (SOI) on the spin textures[24–29]. This novel approach becomes an alternative way since SOI enables the generation and manipulation of spin solely by electric fields or strain effect. Especially, the Rashba effect [25] attracted much attention because it plays an important role in the spintronics device operation such as the spin-field effect transistor (SFET) [29]. On the other hand, current-induced spin polarization [30] and spin Hall effect [31] are the important examples in spintronics where the SOI has a crucial contribution.

Finally, a part from generation and manipulation of spin polarization, another essential requirement for spintronics devices is a long spin lifetime. Here, a new system known as a persistent spin helix (PSH) atracted much attention [32–39]. In this system, the strongly enhanced spin lifetime is achieved on a certain spatially inhomogeneous spin polarization states [32]. As a result, an efficient spintronics devices is believed to be achieved, suggesting that this system is suitable for energy-saving spintronics devices. However, the discovery of the PSH materials has been widely studied only for the zinc-blende semiconductors [32–39]. Therefore, finding another class of materials which is promising candidate for PSH is crucially important in order to realize the PSH based spintronics.

## 1.2 Spin orbit interaction (SOI): A new perspective of spintronics

Recently, the new scheme of spintronics incorporating the effect of spin-orbit interaction (SOI) has been proposed [24–29]. Here, the SOI plays an important role

since it relies to coupling between spin dynamics of an electron and its orbital motion in space. Intuitively, the SOI is a relativistic effect in which an electric field that acts on a fast moving electron is viewed as an effective magnetic field in the reference frame of the electron. Since the SOI induces an effective magnetic field, this study is also known as spintronics without magnetism [24]. In chapter 2, we will present more detail and formal description about the SOI.

In solid state system, the SOI is induced by electric field originated from the lack of space inversion symmetry. Two main cases responsible for lossing the space inversion symmetry: (i) structural inversion asymmetry (SIA) and (ii) bulk inversion asymmetry (BIA). The SIA is induced by the asymmetry of confinement potential of the two dimensional electron gas system in the heterostructures or interface or simply by the presence of surface in a semi-infinite crystal system. The SOI which is induced by the SIA known as Rashba SOI [25]. On the other hand, BIA which originates from the non-centrosymmetric structure of the crystal induces so called Dresselhauss SOI [28].

In the case of system having both BIA and SIA, it is expected that both Rashba and Dresselhauss types appears. For example, in the two dimensional electron gas (2DEG) system realized on the heterostructure of zinc-blende quantum well (QWs), both Rashba and Dresselhauss SOI are identified, which can be effectively controlled by using an externally electric field via gate voltage [25–27, 29] or by introducing strain effect [40]. Furthermore, it is possible to achieved the condition that the contribution of Rashba and Dresselhauss SOI are equal, which induces a well-known persistent spin helix (PSH), exhibiting the strongly enhanced spin lifetime [32–39]. This situation is in fact observed experimentally in the various zinc-blende QWs system [33–39].

## 1.3 An overview of spintronics devices based on SOI

In the spintronics device applications, the ability to utilize and controll spin electron is required. Here, generating of spin-polarized currents is one of the central issue [1, 2]. In semiconductors, the generation of spin polarized currents can be realized by using current injection from ferromagnetic materials [16, 17]. Another

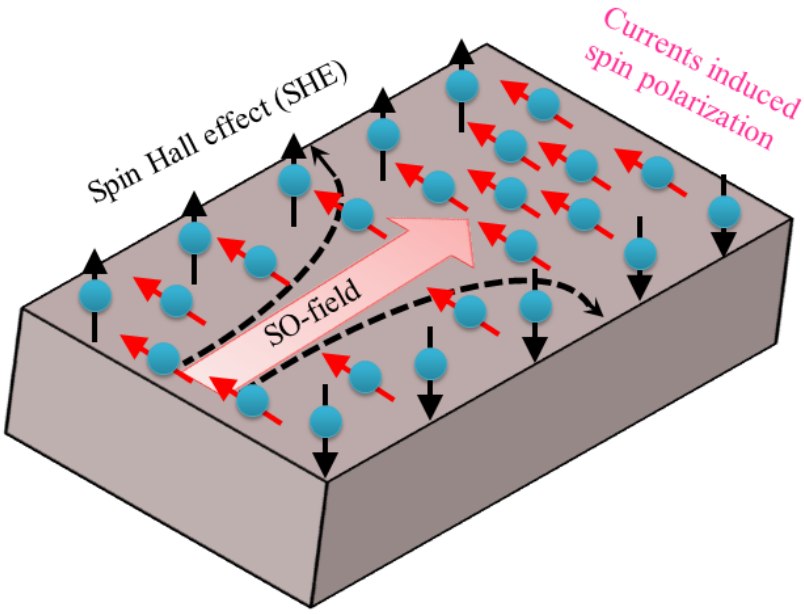


FIGURE 1.1: Generation of spin polarization involving the effect of SOI. Electrically injected electron becomes spin polarized through two mechanism: (i) spin Hall effect (Black arrows) and (ii) currents-induced spin polarization (red arrows).

methods is by using externally applied magnetic fields, which acts as a spin filters to change the unpolarized input currents to be spin-polarized output currents [1, 2]. However, application of external magnetic field in the nonmagnetic system induces stray magnetic field which negatively affects to the spins itself. To overcome this problem, the non-magnetic system which utilize SOI has recently been proposed. In this case, two important mechanism for generating of spin polarized currents have been used such as current induced spin polarization [30] and spin Hall effect [31].

Figure 1.1 shows schematic view of generation spin polarized currents involving the SOI. In semiconductors, electrically-injected electrons become spin polarized through two different mechanisms. First, electron experiences anisotropic scattering from impurity in the presence of SOI, inducing spin accumulation at opposite edges channels with opposite spin direction (black arrows). This mechanism is known as spin Hall effect. The second mechanism, on the other hand, is just currents-induced spin polarization. Here, symmetry-related spin-orbit field produces a homogeneous electron spin polarization throughout the channel(red arrows).

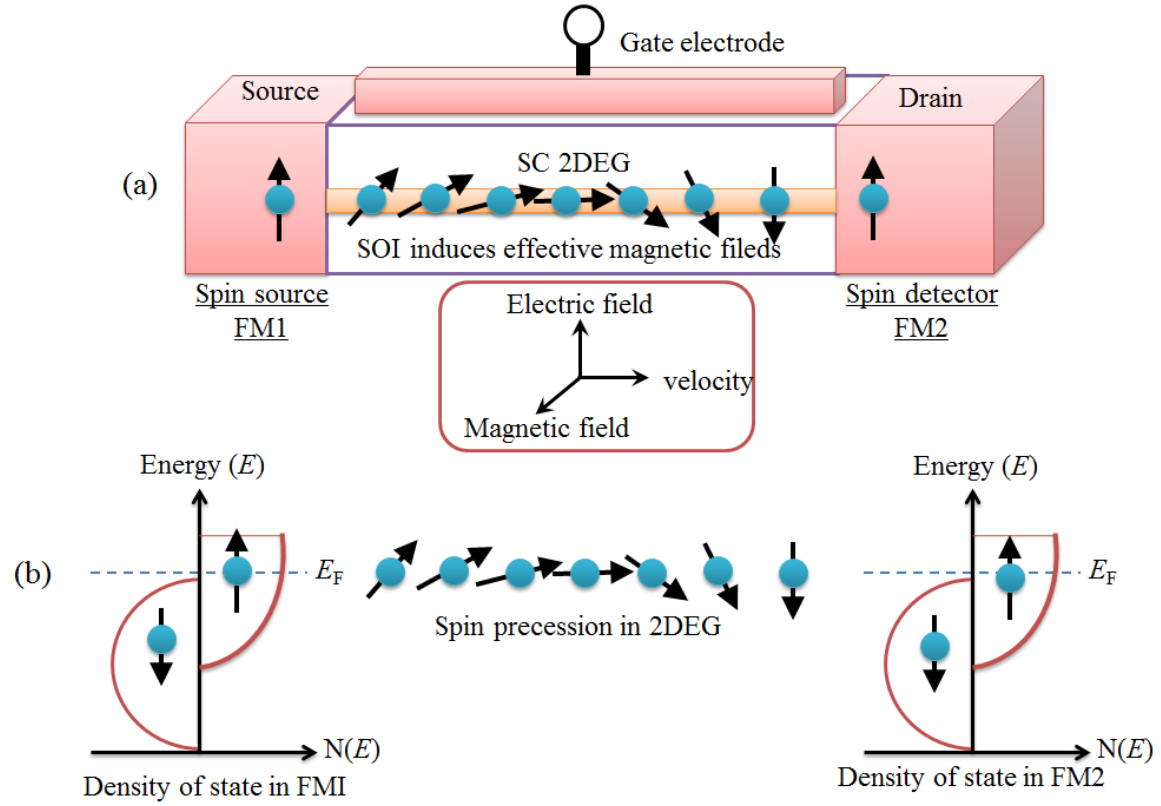


FIGURE 1.2: (a) Prototype of spin field effect transistor proposed by Datta and Das [29]. (b) Mechanism of the spin precession which is induced by SOI. This spin precession can be controlled by applying gate voltage.

Another important issue in spintronics is the manipulation of spin in semiconductors. Here, the application of external magnetic field becomes one of the methods often used [1, 2]. For a more scalable system, it would be desirable if the SOI is used, which is realized by applying an externally electric field originated from the gate electrode [26, 27, 29] or by introducing strain [40]. In this methods, the tunability of spin manipulation can be realized, which gives an advantage for the future device applications.

The realization of the generation and manipulation of spin by using SOI can be found in the spin-field effect transistor (SFET) device, which is firstly proposed by Datta and Das in 1990 [29]. The idea of this proposal is to inject spin-polarized electrons from a ferromagnetic contact into a one dimensional semiconductor channel in which the electrons travel ballistically to the detection contact. As shown in Fig. 1.2(a), the injected electron originates from feromagnetic source electrode (FM1) starts to rotate because of an effective magnetic field induced by SOI in the 2DEG channel. The electrons can flow when the spin orientation in the 2DEG

is aligned to thos of ferromganetic drain electrode (FM2). On the other hand when spin is flipped in the 2DEG, the electron cannot enters the drain electrode since there is no spin flipped in this electrode [Figure 1.2(b)]. Since the SOI can be effectively tuned by the gate voltage, this indicates that the spin precession is controllable.

## 1.4 The purpose: ZnO as a promising material for spintronics

Recently, finding new materials which is suitable as a platform for spintronics applications attracted much scientific interest [1, 2]. One of the systems which can be used as an ideal platform for spintronics is two dimensional electron gas (2DEG) system since it can be controlled by an external electric field or by using strain effect. The zinc-blende semiconductor heterostructures supporting 2DEG system becomes one of the promising materials. For example, various 2DEG saterials such as GaAs/AlGaAs [41, 42] and InGaAs/InAlAs [43] heterostructures has been extensively studuied.

The other class of materials which demonstrating 2DEG system comes from oxide interface system. This is including $LaMnO_3/SrMnO_3$ [44], $GaTiO_3/SrTiO_3$ [45], $LaAlO_3/EuO$ [46], and $LaAlO_3/FeS_2$ [47] in which spin polarized 2DEG has been studied. However, this system has low carrier mobility which is due to the high effective mass of the localized $d$ bands. Therefore, it is not desirable to use this kind of materials as a particular spintronics application such as high electron mobility transistor (HEMT).

Recently, a different system supporting a 2DEG, wurtzite ZnO interface, has been experimentally observed. Observations of the quantum Hall effect [49] and the fractional quantum Hall effect [50] indicate that ZnO/Zn(Mg)O interface has high quality of the two-dimensional electron gas (2DEG). The high carrier concentrations (up to $10^{13}$ $cm^{-2}$) and the high mobility (larger than $10^5$ $cm^2 \cdot V^{-1} \cdot s^{-1}$) at low temperature have been reported [50]. Furthermore, the fabrication of the two dimensional electron gas system was also realized in samples grown with metal-organic vapor deposition, which is suitable for mass production [51].

Considering the fact that ZnO-based materials exhibiting the high quality of the 2DEG system, their application as a spintronics materials is plausible. This is supported by the fact that the spin polarization of the 2DEG in ZnO/Zn(Mg)O has been studied [52] and the long spin lifetime has been observed [53, 54]. However, due to the large ionicity and cryatal symmetry, ZnO posses large internal electric fields. This is in fact strongly different compared to the other materials such as zinc-blende semiconductors. Therefore, for spintronics applications, clarification of the SOI in this material is crucially important, which is expected to induce new useful properties for spintronics.

## 1.5 Outline of Dissertation

This dissertation consists of five chapters. In chapter 1, we present the motivation of this study which is related to the spintronics in general. The new scheme of spintronics based on the spin-orbit interaction (SOI) is given including the generation and manipulation of spin. Here a simple mechanism of the spintronics devices is shown, which is realized on the spin-field effect transitor (SFET).

In chapter 2, we present the basic concepts of the SOI based on the two dimensional electron gas (2DEG) system. The fundamental concepts of density functional theory is also presented. Furthermore, We provide the computational scheme, which is related to the practical calculation in this study.

In Chapter 3, we show the calculated results of the SOI on the strained bulk ZnO. Here we show that strain controls SOI in ZnO, where the inversion Rashba spin rotations are identified. We show that the Rashba spin-orbit strength can be effectively controlled by applying the strain. Finally, we discussed the possible application of the present system for spintronics devices.

In chapter 4, we show the calculated results of the SOI on the wurtzite ZnO $(10\bar{1}0)$ surface. We show that the spin textures show quasi-one dimensional orientation, which is similiar to those of persistent spin helix (PSH). The mechanism which explains the origin of the spin textures is proposed. Furthermore, Some of calculation results of important parameter such as the spin-orbit strength and wavelength of PSH are presented and compare with those various zinc-blende semiconductors.

Finally, in chapter 5, we give a summary and explain the future scope such as the SOI on the metallic surface state of hydrogeneted ZnO($10\bar{1}0$) surface.

# Chapter 2

# Background: Basic Theory and Computational Methods

## 2.1 Introduction

In this chapter, we present the basic theory and methods used in the calculation and analyses. Firstly, we present brief review of the theory of spin-orbit interaction (SOI) in solids, which is given in Sec. 2.2. Some of interesting physical phemnomena such as the Rashba effect, Dresselhauss effect, and their interplay inducing persistent spin helix (PSH) are presented. Next, in Sec. 2.3, we give a brief review of the electronic structures calculation based on the density functional theory (DFT). Finally, the computational scheme, which is related to the practical calculation, are introduced in Sec. 2.4.

## 2.2 The spin-orbit interaction (SOI) in solids

Spin-orbit interaction (SOI) is a relativistic effect in which electrons move with a velocity $\vec{v}$ in the influence of electric field $\vec{E}$ created by the nucleus [Figures 2.1]. In the rest frame of the electron, this electric field transforms into a magnetic field

$$\vec{B} = -(\vec{v} \times \vec{E})/c^2, \tag{2.1}$$

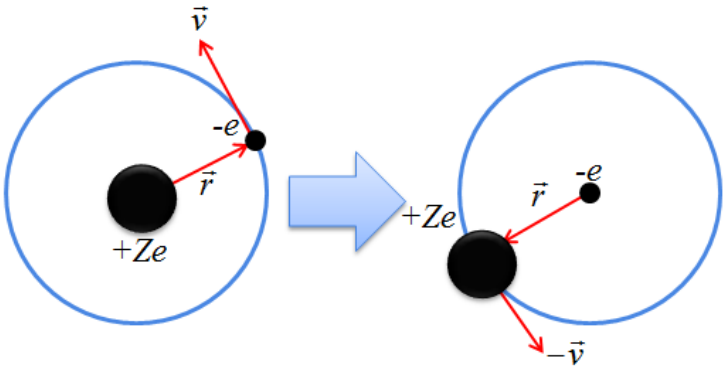


FIGURE 2.1: Schematic view of the relativistic motion of electron in the two difference of reference frame., nuclei (left side) and electron (right side).

where $c$ is the speed of light, that interacts with the magnetic moment $\vec{\mu}$ of the electron. The energy of the electron in this field is given by

$$\Delta E = -\vec{\mu} \cdot \vec{B}. \tag{2.2}$$

Here, $\vec{\mu} = -g_e \mu_B \vec{S}/\hbar$ is the , where $g_e = 2.002$ is the $g$-factor of the electron, $\mu_B = e\hbar/(2m_e)$ is the Bohr magneton, $m_e$ is the electron a free electron, $\hbar$ is Planck's constant, and $\vec{S}$ is the electron spin vector. The SOI, then, can be expressed by,

$$H_{SOI} = -\frac{\hbar}{4m_e^2 c^2} \vec{\sigma} \cdot (\vec{p} \times \vec{E}) \tag{2.3}$$

where $\vec{\sigma} = (\sigma_x, \sigma_y, \sigma_z)$ is the vector of Pauli spin matrices defined as,

$$\sigma_x = \begin{pmatrix} 0 & 1 \\ 1 & 0 \end{pmatrix}, \ \sigma_y = \begin{pmatrix} 0 & -i \\ i & 0 \end{pmatrix}, \ \sigma_z = \begin{pmatrix} 1 & 0 \\ 0 & -1 \end{pmatrix} \tag{2.4}$$

In crystal systems, where the total Hamiltonian is invariant under the time reversal symmetry, the energy solution of the Hamiltonian obeys the relation, $E(\uparrow, \vec{k}) = E(\downarrow, -\vec{k})$, where $\uparrow$ and $\downarrow$ are the up and down spins, respectively. At the same time, the present of the spatial inversion symmetry of crystal induces $E(\uparrow, \vec{k}) = E(\uparrow, -\vec{k})$. Spin degeneracy is the consequence of the combination of the time reversal and spatial inversion symmetry, which leads to the fact that the condition

$E(\uparrow, \vec{k}) = E(\downarrow, \vec{k})$ is obtained. This condition is known as Kramers' degeneracy, where the states is non-spin polarized.

When the space inversion symmetry is broken, the spin degeneracy is lifted by the SOI. The loss of space inversion symmetry can either originate from a structural inversion asymmetry (SIA), which induces the Rashba effect [25–27], or from bulk inversion asymmetry (BIA), which induces the Dresselhauss effect [28]. The SIA is induced by the asymmetric confinement potential of the two dimensional electron gas in a semiconductor heterostructure, or simply by the presence of the surface in a semi-infinite crystal, while the BIA originates from the non-centrosymmetric of the crystal structures. In the following section, we will discuss about the Rashba and Dresselhauss types of SOI and their interplay which induces the well-known persistent spin helix (PSH).

### 2.2.1 Rashba Effect

The Rashba effect has been extensively studied on semiconductor heterostructures in which electrons are confined to the interface [25–27]. Another system exhibiting the Rashba effect is the surface, which is extensively studied on the high quality epitaxial metal layers [55–58]. In the two-dimensional electron gas (2DEG) system under the influence of electric field $E_z$ perpendicular to the growth plane (2DEG-plane), the Rashba SOI can be expressed by the effective Hamiltonian

$$H_R = -\frac{\hbar}{4m_e^2c^2}\vec{\sigma}\cdot(\vec{p}\times\vec{E}) = \alpha_R(\sigma_x k_y - \sigma_y k_x) \tag{2.5}$$

where $\alpha_R = -\hbar E_z/(4m_e^2c^2)$ is the Rashba spin-orbit strength, $k_x$ and $k_y$ are wave vectors in the $x$ and $y$ directions, respectively, and $\sigma_x$ and $\sigma_y$ are Pauli matrixes.

### 2.2.2 Dresselhauss Effect

In some crystal system with lack a center of inversion, such as the zinc-blende crystal, the Dresselhaus SOI is induced [28], which is expressed by

$$H_D = \beta_D[k_x\left(k_y^2 - k_z^2\right)\sigma_x + k_y\left(k_z^2 - k_x^2\right)\sigma_y + k_z\left(k_x^2 - k_y^2\right)\sigma_z]. \tag{2.6}$$

Here, $\beta_D$ is the Dresselhauss spin-orbit strength. In semiconductor heterostructures quantum well (QW), where electrons are confined in the $z$- direction to a two dimensional $(x-y)$ plane, the condition that $\langle k_z \rangle = 0$ and $\langle k_z^2 \rangle \approx (\pi/d)^2$ are obtained, where $d$ is the well width. As a result, the Hamiltonian in Eq. (2.7) can be written in the first and third terms of $k$, which is expressed by

$$H_D = \beta_1(k_x\sigma_x - k_y\sigma_y) + \beta_3[k_x k_y^2\sigma_x - k_y k_x^2\sigma_y]. \tag{2.7}$$

where $\beta_1 = \beta_D^{'} = \beta_D(\pi/d)^2$ and $\beta_3 = \beta_D$ are the first and third terms of the Dresselhauss spin-orbit strength, respectively.

### 2.2.3 Interplay between Rashba and Dresselhauss SOI: the persistent spin helix (PSH)

The total Hamiltonian of the SOI incorporated the Rashba and Dresselhauss terms is expressed by

$$H_{SOC} = \alpha_R(\sigma_x k_y - \sigma_y k_x) + \beta_1(k_x\sigma_x - k_y\sigma_y) + \beta_3(k_x k_y^2\sigma_x - k_y k_x^2\sigma_y) \tag{2.8}$$

In this Hamiltonian, the Schrödinger equation leads to the eigenvalues solution in which two energy braches appears, known as apin-split bands $E(\mathbf{k}, \uparrow\downarrow)$. This spin-split bands obey the condition that $E(\mathbf{k}, \uparrow) \neq E(\mathbf{k}, \downarrow)$ for $k \neq 0$, while it requires $E(\mathbf{k}, \uparrow) = E(-\mathbf{k}, \downarrow)$ for $k = 0$ due to the time reversability.

For each $\mathbf{k}$, the spin splitting $\Delta E_{\texttt{split}}(\mathbf{k})$ is defined as

$$\Delta E_{\texttt{split}}(\mathbf{k}) = E(\mathbf{k}, \uparrow) - E(\mathbf{k}, \downarrow). \tag{2.9}$$

For the case of $\beta_3 = 0$, the eigenvalues of Hamiltonian of Eq. (2.7) leads to the band dispersion:

$$E(\mathbf{k}, \uparrow\downarrow) = \frac{\hbar^2 k^2}{2m*} \pm k\zeta(\alpha_R, \beta_1, \theta_{\mathbf{k}}), \tag{2.10}$$

where $\zeta(\alpha_R, \beta_1, \theta_{\mathbf{k}})$ is defined as

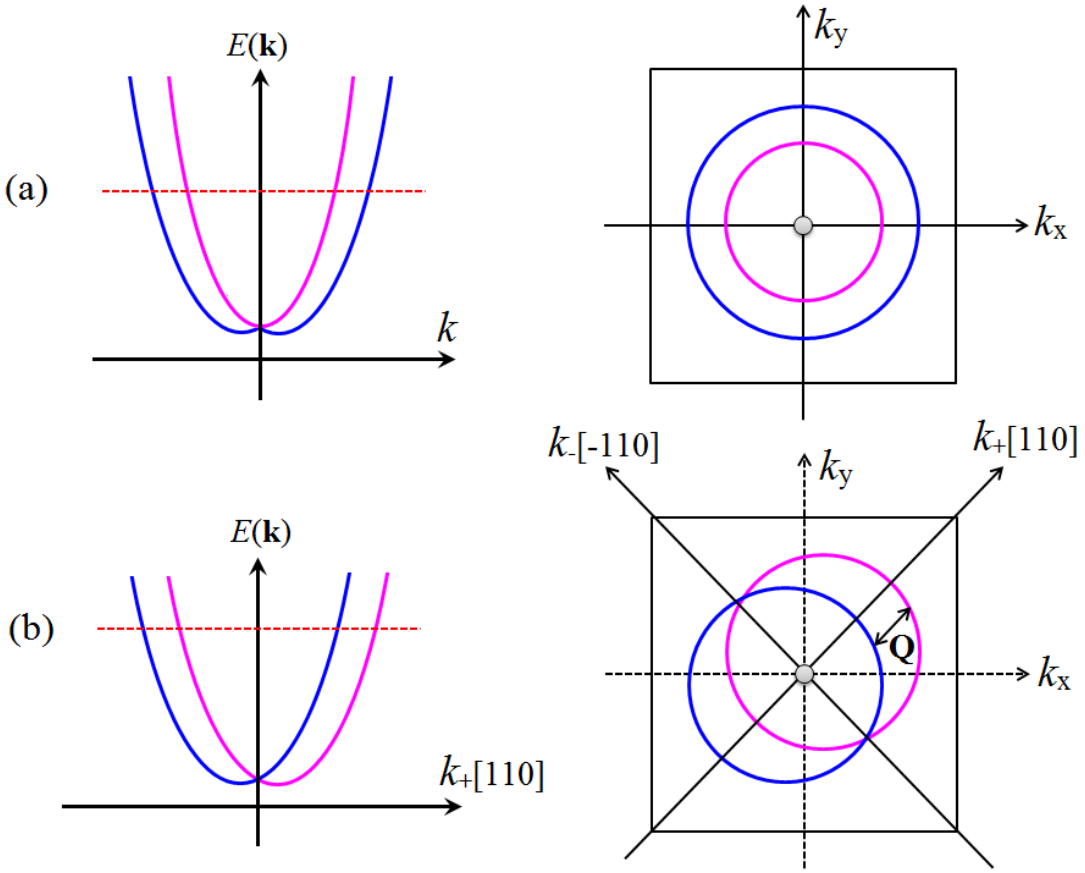


FIGURE 2.2: Schematic representation of the splitting band dispersion and the $k$-surfaces of constant energy for pure Rashba SOI (a) and combination between Rashba and Dresselhauss SOI (b) with the same spin-orbit strength ($\alpha_R = \beta_1$).

$$\zeta(\alpha_R, \beta_1, \theta_{\mathbf{k}}) = \sqrt{\alpha^2 + \beta_1^2 + 2\alpha_R\beta_1 \sin 2\theta_{\mathbf{k}}}. \tag{2.11}$$

In this expression, $\theta_{\mathbf{k}}$ is defined in the $k_x - k_y$ plane by the relation, $\mathbf{k} = (|k| \cos\theta_{\mathbf{k}}, |k| \sin\theta_{\mathbf{k}}$. For the case of pure Rashba SOI, the band dispersion in Eq. (2.10), leads to the well-known Rashba dispersion:

$$E(\mathbf{k}, \uparrow\downarrow) = \frac{\hbar^2 k^2}{2m*} \pm \alpha_R k. \tag{2.12}$$

In this band dispersion, the spin splitting energy, $\Delta E_{\mathtt{split}}(\mathbf{k})$, is linear in $k$ along any direction. This splitting is isotropic where $k$-surfaces of constant energy are concentric circles centered at $k = 0$ [Figure 2.2(a)]. When we introduce the Dresselhauss SOI, on the other hand, the Eq. (2.10) leads to anisotropic of the spin splitting $\Delta E_{\mathtt{split}}(\mathbf{k})$ [Figure 2.2(b)].

An interesting case is obtained when $\alpha_R = \beta_1$. In this case, a novel system called as persistent spin helix (PSH) is achieved [32]. Here, energy band dispersion in Eq. (2.10) reduces to be

$$E(\mathbf{k}, \uparrow\downarrow) = \frac{\hbar^2 k^2}{2m*} \pm 2\alpha_R k_+, \tag{2.13}$$

where $k_+ = (k_x + k_y)/\sqrt{2}$. This PSH band dispersion has the shifting properties,

$$E(\mathbf{k}, \uparrow) = E(\mathbf{k}+\mathbf{Q}, \downarrow). \tag{2.14}$$

Here, $\mathbf{Q} = Q_+ = 4m\alpha_R$ is the shifting wave vector. In this PSH band dispersion, $k$-surfaces of constant energy consist of two circles shifted by the wave vector $\mathbf{Q}$ [Figure 2.2(b)].

The eigen energies of $E(\mathbf{k}, \uparrow\downarrow)$ in Eq. (2.10) corresponds to the eigenstate [59]

$$\Psi(\mathbf{k}, \uparrow\downarrow) = \frac{\exp(i(\mathbf{k}\cdot\mathbf{r}))}{\sqrt{2}} \begin{pmatrix} i\exp(-i\varphi(\mathbf{k})) \\ \pm 1 \end{pmatrix} \tag{2.15}$$

where the function $\varphi(\mathbf{k})$ obeys the relation,

$$\exp(-i\varphi(\mathbf{k})) = \frac{\alpha_R \exp(-i\theta_{\mathbf{k}}) - i\beta_1 \exp(-i\theta_{\mathbf{k}})}{\zeta(\alpha_R, \beta_1, \theta_{\mathbf{k}})} \tag{2.16}$$

Subsequently, by using Eq. (2.15) the spin polarization can be evaluated by calculating the expected value of spin using the expression,

$$P^{\uparrow\downarrow} = \langle \Psi(\mathbf{k}, \uparrow\downarrow) | S | \Psi(\mathbf{k}, \uparrow\downarrow) \rangle = \begin{pmatrix} \mp \sin\varphi(\mathbf{k}) \\ \pm \cos\varphi(\mathbf{k}) \\ 0 \end{pmatrix} \tag{2.17}$$

For the case of pure Rashba SOI, we have $\varphi(\mathbf{k}) = \theta_{\mathbf{k}}$. In this case, the spin polarization in Eq. (2.17) leads to the expression

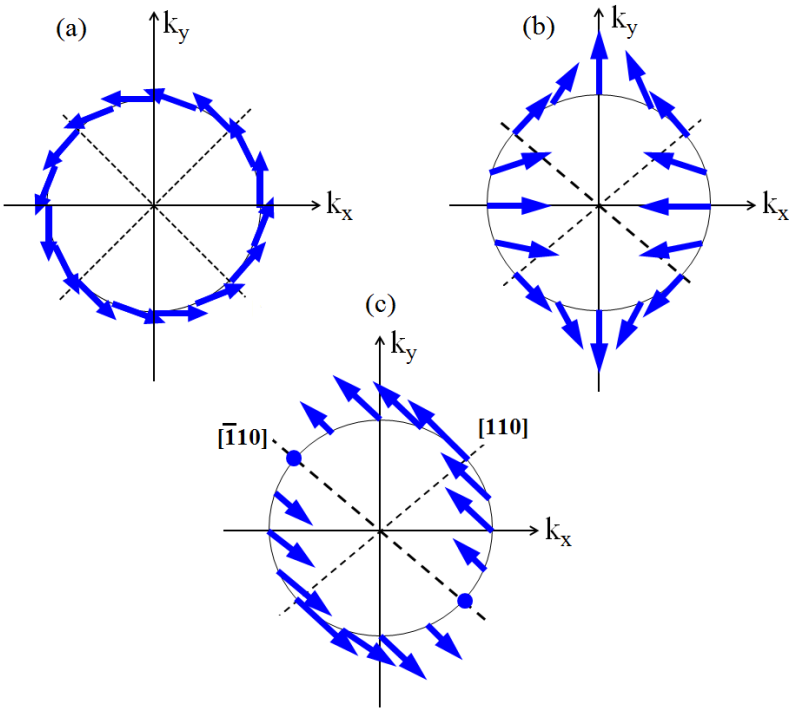


FIGURE 2.3: Schematic representation of the spin polarization for pure Rashba SOI (a), Dresselhauss SOI (b), and persistent spin helix (c).

$$P^{\uparrow\downarrow} = \begin{pmatrix} \mp \sin\theta_{\mathbf{k}} \\ \pm \cos\theta_{\mathbf{k}} \\ 0 \end{pmatrix} \tag{2.18}$$

In the case of PSH ($\alpha_R = \beta_1$), we find that $\varphi(\mathbf{k}) = \pi/4$, then the spin polarization in Eq. (2.17) leads to the form

$$P^{\uparrow\downarrow} = \begin{pmatrix} \mp \frac{1}{\sqrt{2}} \\ \pm \frac{1}{\sqrt{2}} \\ 0 \end{pmatrix} \tag{2.19}$$

Figure 2.3 shows the spin polarization for several cases. For the case of pure Rashba or Dresselhauss SOI, the spin polarization is $k$-dependent [Figure 2.3 (a) and (b)]. this leads to the fact that the spin polarization decays implying the shorter spin relaxation time. On the other hand, in the case of PSH, the spin polarizations show one dimensional orientation, which is independent to $k$ [Figure 2.3 (c)]. This leads to the fact that spins do not precess, suppresing the decay of spin polarization, which induces the strongly enhanced spin relaxation time [32].

### 2.2.4 Spin relaxation time

One of the important consequences of SOI is the spin relaxation time. In the classical picture of the electron, a single spin $\vec{s}_{\vec{k}}$ propagates along certain direction with the velocity $\frac{\hbar\vec{k}}{m}$ and precesses around magnetic field $\vec{B}_{\vec{k}}$ induced by the spin-orbit interaction (SOI), the precession of the ballistically propagating single spin is expressed by

$$\frac{d\vec{s}_{\vec{k}}}{dt} = \vec{\Omega}_{\vec{k}} \times \vec{s}_{\vec{k}} \tag{2.20}$$

where $\vec{\Omega}_{\vec{k}}$ is the precession frequency defined as $\vec{\Omega}_{\vec{k}} = \frac{g\mu_B \vec{B}_{\vec{k}}}{\hbar}$. The term of $\vec{B}_{\vec{k}}$ in the precession frequency can be understood by expressing the SOI Hamiltonian in term of Zeeman spin splitting,

$$H_{SOI} = \frac{g\mu_B \vec{B}_{\vec{k}}}{\hbar} \cdot \vec{S} \tag{2.21}$$

Inserting Eq. (2.21) into Eq. (2.8) and setting that $\beta_3 = 0$, the effective magnetic field can be expressed by

$$\vec{B}_{\vec{k}} = \frac{2k}{g\mu_B} \begin{pmatrix} \alpha_R \sin\theta + \beta_1 \cos\theta \\ -\alpha_R \cos\theta - \beta_1 \sin\theta \end{pmatrix} \tag{2.22}$$

In the case of diffusion limit, where the effective momentum scattering time ($\tau_p^*$) is much smaller than the time for fully spin rotation, the spin travels random walk on the Bloch sphere. In this situation, the spin polarization decays through D'yakonov-Perel' mechanism [60], where the decay rate is expressed as

$$\frac{1}{\tau_x} = \tau_p^* \left\langle \Omega_x^2 \right\rangle \tag{2.23}$$

$$\frac{1}{\tau_y} = \tau_p^* \left\langle \Omega_y^2 \right\rangle \tag{2.24}$$

$$\frac{1}{\tau_z} = \tau_p^* \left\langle (\Omega_x^2 + \Omega_y^2) \right\rangle \tag{2.25}$$

Here, $\tau_x$, $\tau_y$, and $\tau_z$ denote the spin life time for a spin polarization along $x$-, $y$-, and $z$-directions, respectively. For the case of pure Rashba SOI ($\beta_1 = 0$), the Rashba spin-orbit field induces the precession of the spin where the spin life time decreses by increasing of the quadratic $\alpha_R$. This indicates that the large Rashba spin-orbit strength $\alpha_R$ significantly reduces the spin life time. On the contrary, in the case of the persistent spin helix ($\alpha_R = \beta_1$), the effective spin-orbit field is unidirectional, which leads to the fact that the spin do not precess, inducing the strongly enhanced spin life time [32].

## 2.3 Electronic structure based on the density functional theory

In the real system, the simplified Hamiltonian mentioned before cannot describe correctly the effect of SOI. This is due to the fact that the interaction between the electrons and also nuclei plays an important role. Indeed, for the case of materials that contains atoms of high Z (atomic number), SOI has significant contribution of their electronic properties. Since in the complex system, understanding of the SOI involves many body interactions, the study of the electronic properties of the interacting systems is important. Here, the density functional theory (DFT) based methods is the powerfull tool to describe the correct understanding of the electronic properties incorporating the effect of SOI. The brief review of the DFT scheme are given in the following sub-sections.

### 2.3.1 Manybody Problems in condensed Matter

In condensed matter physics, the origin of the various material properties can be understood by identifiying the interaction of electrons. Here, a detailed understanding of electronic structure is the most importance knowledge. To reach detailed knowledge about the electronic structure, a valid quantum-mechanical description of the physical properties of materials is required. In the complex system consisting of many electrons and nuclei, the Schrödinger equation can be expressed as

$$H\Psi(\mathbf{r}_1, \mathbf{r}_2, ..., \mathbf{R}_1, \mathbf{R}_2, ...) = E\Psi(\mathbf{r}_1, \mathbf{r}_2, ..., \mathbf{R}_1, \mathbf{R}_2, ...) \tag{2.26}$$

where $\Psi$ is the wave function of the system, $\mathbf{r}_i$ and $\mathbf{R}_i$ are the positions of the electrons and ions respectively, and $H$ is the Hamiltonian of the system, which is expressed in the form

$$H = -\sum_i \frac{\nabla_i^2}{2} - \sum_{i,I} \frac{Z_I}{|\mathbf{r}_i - \mathbf{R}_I|} + \frac{1}{2}\sum_{i \neq j} \frac{1}{|\mathbf{r}_i - \mathbf{r}_j|} - \sum_I \frac{\nabla_I^2}{2M_I} + \frac{1}{2}\sum_{I \neq J} \frac{Z_I Z_J}{|\mathbf{R}_i - \mathbf{R}_j|} \quad (2.27)$$

where $M_I$ and $Z_I$ are the nucleus mass and charge, respectively. Here, we use the atomic units, where $\hbar = m_e = e = 4\pi\epsilon_0 = 1$. Furthermore, the Hamiltonian in Eq. (2.27) can be decomposed into five terms

$$H = T_{el} + V_{el-nuc} + V_{el-el} + T_{nuc} + V_{nuc-nuc} \quad (2.28)$$

where $T_{el}$ and $T_N$ are the kinetic energy operator of electrons and nuclei respectively, $V_{el-nuc}$ is the potential energy of the electrons relative to the nuclei, $V_{el-el}$ represents the Coulomb interaction between the electrons, and similarly, $V_{nuc-nuc}$ is the Coulomb interaction between nuclei.

The Eq. (2.26) is defined in $3M + 3N$-parameter space dimension, which is too complex to be solved except for the simplest system such as the hydrogen atom. For the larger systems such as molecules and solids, additional approximations have to be used. Considering the fact that the mass of the nuclei is much larger than those of the electron, the motion of nuclei is negligible compared to those of the electrons. Therefore, from the electron point of view, the nuclei move stationary and fix their positions. This approximation is known as the Born-Oppenheimer approximation.

In this approximation, $T_N$ and $V_{nuc-nuc}$ in Eqs. (2.28) can be ignored and the Hamiltonian in Eq. (2.28) can be simplfied by

$$H = T_{el} + V_{el-el} + V_{el-nuc} \quad (2.29)$$

The Schrödinger equation of this system now can be expressed as

$$H\Psi = \left[ -\sum_i \frac{\nabla_i^2}{2} + \frac{1}{2}\sum_{i \neq j} \frac{1}{|\mathbf{r}_i - \mathbf{r}_j|} - \sum_{i,I} \frac{Z_I}{|\mathbf{r}_i - \mathbf{R}_I|} \right] \Psi = E\Psi \tag{2.30}$$

where $\Psi = \Psi_(\mathbf{r}_1, \mathbf{r}_2, ...)$ is many electron wave function. We can see that the original problem is now reformulated as a quantum many-body problem for the electrons in an Hamiltonian set by the nuclei positions.

### 2.3.2 The Hartree approximation

The simplest method to solve the many-electron equation is to rewrite Eq. (2.29) as a one-particle equation for an electron moving in an average potential of all the electrons. This method is well known as the Hartree approximation [61]. In this methods, the wave function can be written as a product of $n$ independent electron wave functions $\phi(\mathbf{r}_n)$ as follows

$$\Psi(\mathbf{r}_1, \mathbf{r}_2, ..., \mathbf{r}_n) = \phi(\mathbf{r}_1)\phi(\mathbf{r}_2)...\phi(\mathbf{r}_n) \tag{2.31}$$

By employing the variational principle, if $E_0$ is the ground state energy solution of the the Schrödinger equation, the condition that

$$\frac{\langle \phi \, | H | \, \phi \rangle}{\langle \phi | \phi \rangle} \geq E_0 \tag{2.32}$$

is obtained for any wave function $\phi$. By inserting Eq. (2.31) to Eq. (2.30), we can obtaine the Hartree equation:

$$[-\sum_i \frac{\nabla_i^2}{2} - \sum_{i,I} \frac{Z_I}{|\mathbf{r}_i - \mathbf{R}_I|} + \sum_{i \neq j} \int \phi^* j(\mathbf{r}_j) \frac{1}{|\mathbf{r}_i - \mathbf{r}_j|} \phi_j(\mathbf{r}_j)] \phi_i(\mathbf{r}_i) = \epsilon_i \phi_i^* \mathbf{r}_i. \tag{2.33}$$

In Eq. (2.33), each electron $i$ is treated independently but in an effective potential, which is determined by an integration over the wave function of the other electron.

Since for the $i^{\mathtt{th}}$ wave function, the effective potential depends on all of other wave functions, we can solve Eq. (2.33) by using the self consistent method. In this

methods, the wave function for the step $k$ can be found by solving the Eq. (2.33) with the effective potential is determined by the wave function in step of $k-1$. This procedure is repeated untill all of the wave functions converge to a solution.

### 2.3.3 The Hartree-Fock approximation

In the Hartree approximation, the exchange interaction is not included in the calculation since only symmetric wave functions are used. Therefore, this calculation does not satisfy Pauli exclusion principle. Hartree and Fock in 1926 [62] introduce an approximation methods which deals with electron as a distinguishable particles. Therefore, the system with $n$-electron wave function is approximated by the anti-symmetric wave function, which described by a Slater determinant [63]:

$$\Psi(\mathbf{r}_1, \mathbf{r}_2, ..., \mathbf{r}_n) = \frac{1}{\sqrt{n!}} \begin{pmatrix} \phi_{1(\mathbf{r}_1)} & \phi_{2(\mathbf{r}_2)} & \cdots & \phi_{n(\mathbf{r}_n)} \\ \phi_{1(\mathbf{r}_2)} & \phi_{2(\mathbf{r}_2)} & \cdots & \phi_{n(\mathbf{r}_2)} \\ \vdots & \vdots & \ddots & \vdots \\ \phi_{1(\mathbf{r}_n)} & \phi_{2(\mathbf{r}_n)} & \cdots & \phi_{n(\mathbf{r}_n)} \end{pmatrix} \tag{2.34}$$

By applying variational principle with this Slater determinant, the solution can be obtained by solving the Hartree-Fock equation:

$$[-\sum_i \frac{\nabla_i^2}{2} - \sum_{i,I} \frac{Z_I}{|\mathbf{r}_i - \mathbf{R}_I|} + \sum_{i \neq j} \int \phi^* j(\mathbf{r}_j) \frac{1}{|\mathbf{r}_i - \mathbf{r}_j|} \phi_j(\mathbf{r}_j)] \phi_i(\mathbf{r}_i) - \sum_j [\int \phi^* j(\mathbf{r}_j) \frac{1}{|\mathbf{r}_i - \mathbf{r}_j|} \phi_i(\mathbf{r}_j)] \phi_j(\mathbf{r}_i) = \epsilon_i \phi_i^* \mathbf{r}_i \tag{2.35}$$

It is clearly seen that the new term appears in the Hartree-Fock equation, which is called as a exchange potential. However, in this equation, the correlation energy due to many body interaction is ignored, which produces incorrect description of the electronic properties. Therefore, the methods which incorporates the effect of both exchange and correlation is necessary.

### 2.3.4 The Density Functional Theory Approximation

As mentioned before that the electronic structure of the many body system can be described by incorporating the effect of both exchange and correlation. Therefore, an efficient computational practicable scheme is necessary. Recently, DFT is one of the most popular and successful quantum mechanical approaches to describe matter, which is recently applied for calculating, e.g., the binding energy of molecules in chemistry and the electronic band structure of solids in physics. The idea of DFT is to describe interacting electron system in the form of electron density. This idea is based on the two theorems, which is proposed by Hohenberg and Kohn[64]. The details of the Hohenberg-Kohn are given in the next section.

#### 2.3.4.1 The Hohenberg-Kohn Theorems

There are two theorems porposed by Hohenberg and Kohn[64], which is used as a basis of modern theory of DFT. The first theorem states that the many-body wave functions, which is a central quantity in standar quantum theory, are replaced by using the ground states electron density without any loss of information. This theorem justified that the electron density is the central quantity to find any information of electronic properties. The second theorem give a guidance for the practical computational, which is equaivalent to the variational principles in quantum mechanics.

For the system consists of $n$ electrons, the electron density is defined by using the wave function, which is expressed as

$$n(\mathbf{r}) = \sum_{i=1}^{N} \int \cdots \int d\mathbf{r}_1 \cdots d\mathbf{r}_N \Psi^*(\mathbf{r}_1, \cdots, \mathbf{r}_N) \delta(\mathbf{r}_i - \mathbf{r}) \Psi(\mathbf{r}_1, \cdots, \mathbf{r}_N) \qquad (2.36)$$

This equation leads to the fact that the energy can be rewritten as a functional of electron density but not explicitly the wave function.

The original Hohenberg-Kohn theorems are:

**Theorem 1**. *For any system of interacting particles in an external potential* $V_{ext}(\mathbf{r})$*, the potential* $V_{ext}(\mathbf{r})$ *is determined uniquely, except for a constant, by the ground state density* $n_0(\mathbf{r})$.

This first theorem implies that all of the electronic properties can thus be extracted from the exact ground state electron density. The ground state electron density can be found by applying the second theorem, which is based on the variational principle.

**Theorem 2**. *A universal functional for the energy* $E[n]$ *in terms of the density* $n(\mathbf{r})$ *can be defined, valid for any external potential* $V_{ext}(\mathbf{r})$*. The exact ground state energy of the system is the global minimum of this functional and the density that minimizes the functional is the exact ground state density* $n_0(\mathbf{r})$.

The second theorem reduces the complex problem to find all of ground state physical properties of a system by minimizing the energy with respect to the electron density. The energy functional as expressed by

$$E_{HK}[n] = T[n] + E_{int}[n] + \int V_{ext}(\mathbf{r})n(\mathbf{r})d\mathbf{r} + E_N \tag{2.37}$$

where $E_{HK}[n]$ is the total energy functional, $T[n]$ is kinetic energy part, and $E_{int}[n]$ is the electron interactions energy. In Eq. (2.37) $E_N$ is independent to the density, which is due to the nuclei-nuclei interaction. It should also be noted that using the Hohenberg-Kohn formulation of DFT implies that we are working at T = 0 K.

#### 2.3.4.2 The Kohn-Sham Equations

Kohn-Sham reformulated the problem in a more familiar form, which opens way to the practical applications of DFT. Kohn and Sham have shown that there is a way to map the problem of solving Eq. (2.37) to those of a system with non-interacting electrons under an effective potential contributed from all of the other electrons[65]. According to Theorem 2, the true electron density will minimize the total energy, which could be guessed, or, as suggested by Kohn and Sham, calculated from a reference system of non-interacting electrons moving in an effective potential.

For a system with non-interaction electrons, the ground state charge density is represented as a sum over one-electron orbitals,

$$n(\mathbf{r}) = 2\sum_{i}^{N} |\Psi(\mathbf{r})|^2 , \tag{2.38}$$

where $i$ runs from 1 to $N/2$ for the case of double occupancy of all states. The electron density $n(\mathbf{r})$ can be varied by changing the wave function $\Psi(\mathbf{r})$ of the system.

The Kohn-Sham methods is based on replacing electron interaction by using non-interaction electrons, which is under influence of an effective potential[65]. The effective potential consists of the external potential, the Coulomb interaction between electron, and the exchange and correlation interactions. Therefore, the Kohn-Sham energy functional for the ground state can be expressed by

$$E_{KS}[n(\mathbf{r})] = T_s[n(\mathbf{r})] + E_H[n(\mathbf{r})] + E_{XC}[n(\mathbf{r})] + \int V_{ext} n(\mathbf{r}) d\mathbf{r} \tag{2.39}$$

In Eq. (2.39), The first term is the kinetic energy of non-interaction electrons, which is expressed by

$$T_s[n(\mathbf{r})] = -\sum_{i} \int \Psi_i^*(\mathbf{r}) \nabla^2 \Psi_i(\mathbf{r}) d\mathbf{r}, \tag{2.40}$$

the second term represented the Hartree energy, which is contains the electrostatic interactio between cloud charge, which is defined as,

$$E_H[n(\mathbf{r})] = \frac{1}{2} \int \frac{n(\mathbf{r}) n(\mathbf{r'})}{\mathbf{r} - \mathbf{r'}} d\mathbf{r} d\mathbf{r'}, \tag{2.41}$$

and the third term is the exchange and correlation terms, which are groupped into exchange-correlation energies $E_{XC}$. When all of the functional $E_{XC}[n(\mathbf{r})]$ is known, the exact ground state density and the energy of the many body system can be found.

Considering the fact that the Khon-Sham energy problem is a minimization problem with respect to the density $n(\mathbf{r})$, the solution can be obtained by performing functional derivative as below

$$\frac{\delta E_{KS}}{\delta \Psi_i^*(\mathbf{r})} = \frac{\delta T[n]}{\delta \Psi_i^*(\mathbf{r})} + [\frac{\delta E_{ext}[n]}{\delta n(\mathbf{r})} + \frac{\delta E_H[n]}{\delta n(\mathbf{r})} + \frac{\delta E_{XC}[n]}{\delta n(\mathbf{r})}]\frac{\delta n(\mathbf{r})}{\delta \Psi_i^*(\mathbf{r})} - \frac{\delta(\lambda(\int n(\mathbf{r})d\mathbf{r} - N))}{\delta n(\mathbf{r})}[\frac{\delta n(\mathbf{r})}{\delta \Psi_i^*(\mathbf{r})}] = 0, \tag{2.42}$$

where $\lambda$ is the Lagrange multiplier. In Eq. (2.42), the last term is the Lagrang multiplier for handling the constrain. Therefore, the non-trivial solution can be obtained.

the second term of Eq. (2.32) indicates that all of potentials such as the external, Hartree, and the exchange-correlation potentials are expressed in the form of derivative functional so that

$$V_{\mathtt{ext}} = \frac{\delta E_{ext}[n]}{\delta n(\mathbf{r})},\ V_H = \frac{\delta E_H[n]}{\delta n(\mathbf{r})},\ V_{XC} = \frac{\delta E_{XC}[n]}{\delta n(\mathbf{r})}. \tag{2.43}$$

By setting that

$$\frac{\delta n(\mathbf{r})}{\delta \Psi_i^*(\mathbf{r})} = 2\Psi_i(\mathbf{r}), \tag{2.44}$$

each term in the right side of Eq. (2.42) can be expressed as

$$\frac{\delta T[n]}{\delta \Psi_i^*(\mathbf{r})} = -\nabla^2 \Psi_i(\mathbf{r}), \tag{2.45}$$

$$[\frac{\delta E_{ext}[n]}{\delta n(\mathbf{r})} + \frac{\delta E_H[n]}{\delta n(\mathbf{r})} + \frac{\delta E_{XC}[n]}{\delta n(\mathbf{r})}] = 2(V_{ext} + V_H + V_{XC}(\mathbf{r}))\Psi_i^*(\mathbf{r}) \tag{2.46}$$

$$\frac{\delta(\lambda(\int n(\mathbf{r})d\mathbf{r} - N))}{\delta n(\mathbf{r})}[\frac{\delta n(\mathbf{r})}{\delta \Psi_i^*(\mathbf{r})}] = 2\epsilon_i \Psi_i^*(\mathbf{r}). \tag{2.47}$$

By inserting Eqs. (2.45), (2.46), and (2.47) to Eq. (2.42), we obtained the well-known Kohn-Sham equation

$$[-\frac{1}{2}\nabla^2 + V_{KS}(\mathbf{r})]\Psi_i(\mathbf{r}) = \Psi_i(\mathbf{r}) \tag{2.48}$$

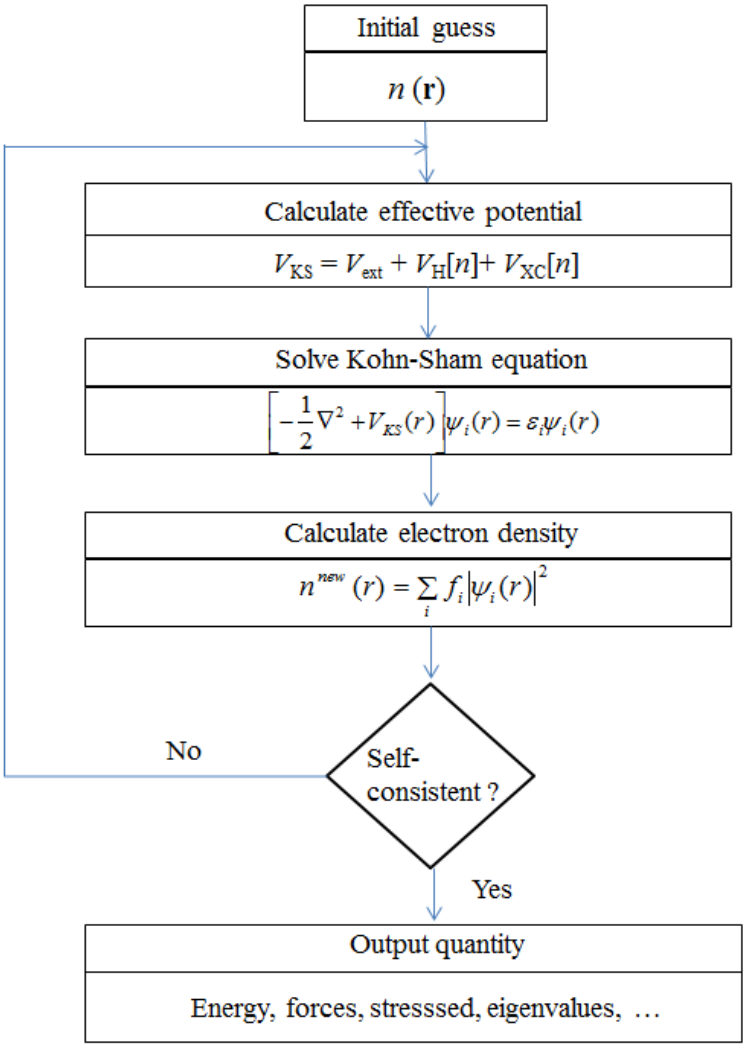


FIGURE 2.4: Schematic representation of the self-consistent loop for solution Kohn-Sham equations.

where

$$V_{KS}(\mathbf{r}) = V_{ext}(\mathbf{r}) + V_H(\mathbf{r}) + V_{XC}(\mathbf{r}) \tag{2.49}$$

Since both $V_{ext}(\mathbf{r})$ and $V_H(\mathbf{r})$ depend on $n(\mathbf{r})$, it is indicate that they also depend on $\Psi_i(\mathbf{r})$. As a result, the problem solving of the Kohn-Sham equation can be obtained by using the self-consistent methods. The self-consistent Kohn-Sham equation is schematically given in Fig. 2.4. It is usually started from an initial guess of $n(\mathbf{r})$, then calculates the corresponding $V_H$ and $V_{XC}$ to obtain $V_{KS}$. Subsequently, the solution of $\Psi_i$ can be obtained by solving the Kohn-Sham equation. From this calculation, a new density, which is obtained by the results of $\Psi_i$, is used as an

initial new guess for $n(\mathbf{r})$, and used to calculate the new $V_{KS}$. This procedure is then repeated untill convergence is reached.

#### 2.3.4.3 The exchange-correlation

In DFT, the mayor problem now is to find the exchange and correlation (XC) energy since their exact functionals are not known except for the free electron gas. Therefore, it is necessary to find an accurate XC energy functional $E_{XC}[n(\mathbf{r})]$ in order to find a satisfactory description of a realistic condensed-matter system. For the case of homogeneous electron system, the functional of $E_{XC}[n]$ depends only on the density. However, in the case of non-homogeneous electron system, the functional of $E_{XC}[n]$ at point $\mathbf{r}$ not only depends on the density at $\mathbf{r}$, but it also depends on the variation at near $\mathbf{r}$.

There many approximation to find an accurate XC energy functionals. The well-known approximations are including the local density approximation (LDA) and the generalized gradient approximation. Next, a brief review of these approximation are given.

**Local Density approximation (LDA)**:

The simplest methods to approximate the exchange correlation energy functional is the local density approximation (LDA). In this approximation two assumptions are made: i) the local exchange-correlation energy per particle only depends on the local density, and ii) is equal to the exchange-correlation energy per particle of a homogeneous electron gas, which has the same density in the neutralizing positive background (jellium background). The total exchange-correlation energy $E_{XC}$ is then given by the sum of the contributions of each point in space, where it is assumed that the contribution of one point only depends on the density of that particular point and it independent of the other points. Therefore, the exchange correlation energy functional can be expressed by

$$E_{XC}[n(\mathbf{r})] = \int n(\mathbf{r})\epsilon_{XC}(n(\mathbf{r}))d\mathbf{r} \tag{2.50}$$

where $\epsilon_{XC}(n(\mathbf{r}))$ is the exchange-correlation energy per particle of a uniform electron gas with density $n(\mathbf{r})$. Furthermore, the quantity $\epsilon_{XC}(n(\mathbf{r}))$ can be split into exchange and correlation contribution,

$$\epsilon_{XC}(n(\mathbf{r})) = \epsilon_X(n(\mathbf{r})) + \epsilon_C(n(\mathbf{r})) \tag{2.51}$$

In Eq. (2.51), the exchange part, $\epsilon_X(n(\mathbf{r}))$, represents the exchange energy of an electron in a homogeneous electron gas and is given by

$$\epsilon_X(n(\mathbf{r})) = -\frac{3}{4}\sqrt[3]{\frac{3n(\mathbf{r})}{\pi}} \tag{2.52}$$

On the other hand, the expression of the correlation contribution at a homogeneous gas is expressed by

$$\epsilon_C(n(\mathbf{r})) = Aln(r_s) + B + r_s(Cln(r_s)) + D \tag{2.53}$$

in the high density limit, and,

$$\epsilon_C(n(\mathbf{r})) = \frac{1}{2}\left(\frac{g_0}{r_s} + \frac{g_1}{r_s^{3/2}} + \ldots\right) \tag{2.54}$$

in the low density limit, where $g_{i=0\texttt{to}n}$ is the constant parameters. In Eqs. (2.53) and (2.55), $r_s = \sqrt[3]{\frac{3n(\mathbf{r})}{\pi}}$ is the Weigner-Seitz radius.

The LDA approximation is more accurate for systems with slowly varying densities, as it is assumed that the density is locally a constant. In general, LDA almost always leads to a correct picture of binding energy trends across the periodic table. Some of physical properties such as the structures, bond lengths, vibrational energies, phonon spectra and other properties are predicted correctly, or with a systematic deviation. However, some of binding energies of solids and molecules are usually overestimated, which leads to an underestimation of the bond lengths. The LDA is also systematically underestimate the band gap.

**Generalized gradient approximation (GGA)**:

In real systems the density varies in the space. Therefore, the rate change of the functional should be included, which can be obtained by adding gradient terms. This approach is called as the gradient-expansion approximation. In this approximation, the gradient-corrections of the form $|\nabla n(\mathbf{r})|$, $|\nabla n(\mathbf{r})|^2$, and $|\nabla n^2(\mathbf{r})|$ is systematically added to the LDA exchange-correlation energy functionals. Moreover

higher-order corrections are exceedingly difficult to calculate and little is known about them. The general form of the exchange-correlation energy functionals in GGA is expressed by

$$E_{XC}[n(\mathbf{r})] = \int \epsilon_{XC}(n(\mathbf{r}), |\nabla n(\mathbf{r})|, |\nabla n^2(\mathbf{r})|) d\mathbf{r} \tag{2.55}$$

## 2.4 Computational Scheme

For the practical implementation of the DFT calculation, we used the OpenMX code[67]. The OpenMX (Open source package for Material eXplorer) code is a software package for nano-scale material simulations based on density functional theories (DFT)[64]. The norm-conserving pseudopotentials[68] and pseudo-atomic localized basis functions[69, 70] are used in our calculation. We carry-out the spin textures calculation by using post-processing calculation after the self-consistent field potential was obtained. We also perform the electric polarization calculation by using Berry phase methods. In this section, a brief description of the methods used in our calculation are presented, which is implemented on the openMX code[67].

### 2.4.1 Norm conserving pseudo-potential

The concept of a pseudo-potential is replacing the effects of the core electrons with an effective potential. The pseudopotential generation procedure starts with the solution of the atomic problem using the Kohn-Sham (KS) approach. When the KS orbitals are obtained from the solution of the Khon-Sham equation, we can classify the distinction between valence and core states. The core states are assumed to change very small, which is due to changes of the environment. As a result, their effect can be replaced by using a model potential derived from the atomic configuration and it is assumed to be transferable. On the other hand, the valence states are seen to oscillate rapidly close to the core regions. By introducing the new potential, the valence states are expected to be smoother.

Let us assume that the core states and the core eigenvalues of Hamiltonian $\mathbf{H}$ are represented by $|\chi_n\rangle$ and $E_n$, respectively. The valence state $|\Psi\rangle$ can be replaced by

using the smooter wave function $|\phi\rangle$ and expands the remaining portion in terms of core states,

$$|\Psi\rangle = |\phi\rangle + \sum_{n}^{\texttt{core}} a_n |\chi_n\rangle \tag{2.56}$$

By taking the inner product of Eq. (2.56) with the core states $|\chi_n\rangle$, and by considering the fact that the valence states $|\Psi\rangle$ is orthogonal to the core states $|\chi_n\rangle$, we have the relation

$$\langle\chi_n|\Psi\rangle = \langle\chi_n|\phi\rangle + \sum_{n}^{\texttt{core}} a_n \langle\chi_m|\chi_n\rangle = 0 \tag{2.57}$$

Now, we can write the right-hand side of Eq. (2.57) in terms of the pseudo-function, $|\phi\rangle$

$$|\Psi\rangle = |\phi\rangle - \sum_{n} \langle\chi_n |\phi| \chi_n\rangle \tag{2.58}$$

By applying the Hamiltonian onto the expression in Eq. (2.58), we get

$$\mathbf{H}|\Psi\rangle + \sum_{n}(E - E_n)|\chi_n\rangle\langle\chi_n|\phi\rangle = E|\phi\rangle \tag{2.59}$$

It is seen that the smooth pseudo-wave function satisfies an effective equation with the same eigen energy of the real valence wave function. Therefore, Eq. (2.59) can be written in the new eigenvalues equation for the *smooth pseudo wavefunction* $|\phi\rangle$ as

$$(\mathbf{H} + V_{n,l})|\phi\rangle = E|\phi\rangle \tag{2.60}$$

where $V_{n,l}$ depends on the angular momentum quantum number $l$ due to the spherical symmetry and its effect is localized to the core. Since $E > E_n$, this means that this is a repulsive potential, which partially cancels the effect of the attractive Coulombic potential. The resulting potential is then a much weaker than that of the original potential. This indicates that the eigenstates of this new potential are smoother.

In the OpenMX code[67], the non-conserving pseudo potential is used. In this kind of pseudo potential, some requirements are used:

(i) All the electrons (AE) and pseudo (PS) valence eigenvalues are the same as the selected atomic configuration:

$$\epsilon_i^{AE} = \epsilon_i^{PS}. \tag{2.61}$$

(ii) All the electrons (AE) and pseudo (PS) valence eigenvalues are in agreement in the external core region:

$$\Psi_i^{AE}(r) = \Psi_i^{PS}(r),\ r \geq r_c. \tag{2.62}$$

(iii) The logaritmic derivatives and their first energy derivative of real and pseudo wave functions agree for all $R \leq r_c$

$$\left[\frac{d}{dr} \ln \Psi_i^{AE}(r)\right]_R = \left[\frac{d}{dr} \ln \Psi_i^{PS}(r)\right]_R \tag{2.63}$$

(iv) The total charge inside the core radius $R < r_c$ for each wave function must be same, which is due to the norm conservation.

$$\int_0^R \left|\Psi_i^{AE}(r)\right|^2 dr = \int_0^R \left|\Psi_i^{PS}(r)\right|^2 dr \tag{2.64}$$

In the OpenMX code[67], the procedure for the generation of the non-conserving pseudo-potentials for the valence states follows the methods proposed by Troullier and Martin [68]. In this methods, a parametrized analytical function for the core region is choosen as $\phi_{n,l}^{PS} \approx e^{p(r)}$, where $p(r)$ is a six-order polynomial matching the true solution and its various derivatives at $r_c$.

### 2.4.2 The pseudo-atomic basis orbitals

In the OpenMX code[67], the Kohn-Sham wave functions $\Psi_\mu$ are expanded by the linear pseudo atomic orbitals (LPAO) $\phi_{i,\alpha}$[69], which is expressed as

$$\Psi_\mu(\mathbf{r}) = \sum_{i,\alpha} c_{\mu,i,\alpha}\phi_{i,\alpha}(\mathbf{r} - \mathbf{r}_i) \tag{2.65}$$

where $i$ is the site index, $\alpha \equiv (p, l, m)$ is the orbital index, and $\phi_{i\alpha} \equiv Y_{l,m}(\theta, \phi)R_{i,p,l}(r)$. Here, the radial wave function $R_{i,p,l}(r)$ depends on the angular quantum number $l$, the site index $i$, and the multiplicity index $p$. Subsequently, this radial wave functionis is called as a primitive orbitals.

The primitive orbitals $R_{i,p,l}(r)$ can be generated by using the following conditions[69, 70]:

(i) The atomic orbitals must completely vanish within a cutoff radius. They should be continuous up to the third derivatives around the cutoff radius so that matrix elements for the kinetic operator are also continuous up to the first derivatives.

(ii) A few parameters can be used to generate as many as possible a set of atomic orbitals.

Since the primitive orbitals are orbitals of eigenstates of an atomic Kohn-Sham equation with a confinement pseudopotential, they can be vanished in the region which is in the outside of the confinement radius $r_c$. Here, the atomic core potential $V_{core}(r)$ in the all electron calculation can be modified in the generation of pseudopotential, which is mathematically expressed by [69, 70]

$$V_{core}(r) = \begin{cases} -\frac{Z}{r} & \text{for } r \leq r_1; \\ \sum_0^3 b_n r^n & \text{for } r_1 < r \leq r_c; \\ h & \text{for } r_c < r, \end{cases} \tag{2.66}$$

where $b_0$, $b_1$, $b_2$, and $b_3$ are constants, which is determined in the condition that the value and the first derivative are continues at both $r_1$ and $r_c$.

### 2.4.3 Non-collinear DFT

In our calculation, we use non-collinear DFT methods to investigate the effect of spin-orbit interaction (SOI). In the non-collinear DFT, two components spinor wave functions is expressed by

$$|\Psi_v\rangle = |\Psi_v^\alpha \alpha\rangle + \left|\Psi_v^\beta \beta\right\rangle \tag{2.67}$$

where $|\Psi_v^\alpha \alpha\rangle \equiv |\Psi_v^\alpha\rangle\,|\alpha\rangle$ with a spatial function $|\Psi_v^\alpha\rangle$ and a spin function $|\alpha\rangle$. By using this wave functions, the density operator is given by the relation

$$\hat{n} = \sum_v f_v\,|\Psi_v\rangle\,\langle\Psi_v| = \sum_v f_v \left(|\Psi_v^\alpha \alpha\rangle + \left|\Psi_v^\beta \beta\right\rangle\right)\left(|\Psi_v^\alpha \alpha\rangle + \left|\Psi_v^\beta \beta\right\rangle\right) \tag{2.68}$$

Here, $f_v$ is the step function, where in the OpenMX code [67], it is replaced by the Fermi distribution function. By using Eq. (2.68), a non-collinear electron densityin real space is given by

$$n_{\sigma\sigma'} = \langle r\sigma|\hat{n}|r\sigma'\rangle = \sum_v f_v \Psi_v^\sigma \Psi_v^{\sigma',*} \tag{2.69}$$

where $(\sigma, \sigma' = (\alpha, \beta)$ and $|r\rangle$ is a eigenfunction of position vector.

Next, we calculate the up- and down-spin densities $n'_\uparrow$, $n'_\downarrow$ at each point by diagonalzing a matrix consisting of a non-collinear densities:

$$\begin{pmatrix} n'_\uparrow & 0 \\ 0 & n'_\uparrow \end{pmatrix} = UnU^\dagger = U \begin{pmatrix} n_{\alpha\alpha} & n_{\alpha\beta} \\ n_{\beta\alpha} & n_{\beta\beta} \end{pmatrix} U^\dagger. \tag{2.70}$$

Here, the $U$-matrix in Eq.(2.70) is expressed by a rotation operator $D$ [71]:

$$D \equiv \exp\left(-i\hat{\sigma}_i \cdot \hat{h}\phi/2\right) \tag{2.71}$$

where $\sigma_i$ is Pauli matrices defined as

$$\sigma_1 = \begin{pmatrix} 0 & 1 \\ 1 & 0 \end{pmatrix},\ \sigma_2 = \begin{pmatrix} 0 & -i \\ i & 0 \end{pmatrix},\ \sigma_3 = \begin{pmatrix} 1 & 0 \\ 0 & -1 \end{pmatrix} \tag{2.72}$$

In Eq. (2.70), $\hat{h}$ is a unit vector along certain direction, and $\phi$ is a rotational angle around $\hat{h}$. For the rotation along the $z$-axis with Euler angle $(\theta, \phi)$, operator $D$ leads to the matrix:

$$D(\theta,\phi) = \begin{pmatrix} \exp\left(-i\frac{\phi}{2}\right)\cos\left(\frac{\theta}{2}\right) & -\exp\left(-i\frac{\phi}{2}\right)\sin\left(\frac{\theta}{2}\right) \\ \exp\left(i\frac{\phi}{2}\right)\sin\left(\frac{\theta}{2}\right) & \exp\left(i\frac{\phi}{2}\right)\cos\left(\frac{\theta}{2}\right) \end{pmatrix}. \tag{2.73}$$

The $U$-matrix can be found by the conjugate transposed matrix of $D(\theta,\phi)$, which explicitly has the form

$$U = \begin{pmatrix} \exp\left(i\frac{\phi}{2}\right)\cos\left(\frac{\theta}{2}\right) & \exp\left(-i\frac{\phi}{2}\right)\sin\left(\frac{\theta}{2}\right) \\ -\exp\left(i\frac{\phi}{2}\right)\sin\left(\frac{\theta}{2}\right) & \exp\left(-i\frac{\phi}{2}\right)\cos\left(\frac{\theta}{2}\right) \end{pmatrix}. \tag{2.74}$$

By using Eq.(2.67), Eq.(2.69), and Eq.(2.70), the total energy non-collinear functional can be written as [72, 73]

$$E_{\mathtt{tot}} = \sum_{\sigma=\alpha,\beta}\sum_{v} f_v \left\langle \Psi_v^{\sigma}|\hat{T}|\Psi_v^{\sigma}\right\rangle + \sum_{\sigma\sigma'}\int w_{\sigma\sigma'} n_{\sigma\sigma'} + \frac{1}{2}\int\int \frac{n'(\mathbf{r})n'(\mathbf{r'})}{|\mathbf{r}-\mathbf{r}'|}dvdv' + E_{\mathtt{XC}}\left\{n_{\sigma\sigma'}\right\} \tag{2.75}$$

In this Equation, the first and the second terms are represented the kinetic energy and the electron-core Coulomb energy, respectively. Meanwhile, the third and the fourth terms define the electron-electron Coulomb energy and the exchange-correlation energy, respectively. Here, $n'$ at each point is the sum of up- and down-spin densities $n'_{\uparrow}$, $n'_{\downarrow}$. Therefore, Eq. (2.75) can be simplified becomes

$$E_{\mathtt{tot}} = E_{\mathtt{band}} - \frac{1}{2}\int n' V_H dv - \int \mathtt{Tr}(V_{\mathtt{XC}} n)dv + E_{\mathtt{XC}} \tag{2.76}$$

where $V_{\mathtt{XC}}$ is a non-collinear exchange-correlation potential.

Now, we introduce a new functional $\mathtt{F}$ which relates to the orthoganility of the spinor wave functions expressed by

$$\mathtt{F} = E_{\mathtt{Tot}} + \sum_{\sigma\sigma'}\epsilon_{\sigma\sigma'}(\delta_{\sigma\sigma'} - \langle\Psi_v|\Psi_{v'}\rangle). \tag{2.77}$$

The variation of $\mathtt{F}$ with respect to the spatial wave functions $\Psi_u^{\sigma}$ can be written as

$$\frac{\delta \mathtt{F}}{\delta \Psi_u^{\sigma,*}} = \hat{T}\Psi_u^{\sigma} + \sum_{\sigma'} w_{\sigma\sigma'}\Psi_u^{\sigma'} + V_H\Psi_u^{\sigma} + \sum_{\sigma'} V_{\mathtt{XC}}^{\sigma\sigma'}\Psi_u^{\sigma'} - \sum_{v}\epsilon_{uv}\Psi_v^{\sigma} \tag{2.78}$$

with

$$V_H = \int \frac{d\mathbf{r}}{|\mathbf{r} - \mathbf{r'}|} dv \tag{2.79}$$

and

$$V_{\mathtt{XC}}^{\sigma\sigma'} = \frac{\delta E_{\mathtt{XC}}}{\delta n_{\sigma\sigma'}} \tag{2.80}$$

Here, the functional of F becomes minimum if its variation with respect to the spatial wave functions $\Psi_u^\sigma$ vanishes. By using a unitary transfromation of spatial wave functions $\Psi_v^\sigma$ to diagonalize $\epsilon_{uv}$, we obtaine the non-collinear Kohn-Sham equation as follows:

$$\begin{pmatrix} \hat{T} + w_{\alpha\alpha} + V_H + V_{\mathtt{XC}}^{\alpha\alpha} & w_{\alpha\beta} + V_{\mathtt{XC}}^{\alpha\beta} \\ w_{\beta\alpha} + V_{\mathtt{XC}}^{\beta\alpha} & \hat{T} + w_{\beta\beta} + V_H + V_{\mathtt{XC}}^{\beta\beta} \end{pmatrix} \begin{pmatrix} \Psi_u^\alpha \\ \Psi_u^\beta \end{pmatrix} = \epsilon_u \begin{pmatrix} \Psi_u^\alpha \\ \Psi_u^\beta \end{pmatrix} \tag{2.81}$$

It is clearly seen from above equation that a direct interaction between $\alpha$ and $\beta$ spin components couples in the off-diagonal part. Here, the off-diagonal consists of the exchange-correlation potential $V_{\mathtt{XC}}$ and the other new contributions $w$. For example if the spin-orbit interaction (SOI) is included, this will contribute to the new contribution of $w$.

### 2.4.4 The spin textures calculations

When we include the SOI in the self-consistent calculation of the non-collinear Kohn-Sham equation Eq. (2.81), we can obtaine the final spin structures of our system. These final spin structures are then called as spin textures. After self-consistent field potential is obtained [74] from DFT calculations, we can evaluate the spin textures by using the $k$-space spin density matrices of the spinor wave functions, $n_{\alpha\beta}(\mathbf{k}, \mu)$, using the relation:

$$n_{\alpha\beta}(\mathbf{k}, \mu) = \langle \Psi_\alpha(\mathbf{r}, \mathbf{k}, \mu) | \Psi_\beta(\mathbf{r}, \mathbf{k}, \mu) \rangle \tag{2.82}$$

where $\mathbf{r}$, $\mathbf{k}$, and $\mu$ are the position vector, the wave vector, and the band index, respectively. In this expression, $\Psi_\alpha$ and $\Psi_\beta$ are the spinor wave function for up $\uparrow$ and down $\downarrow$ spins, respectively, which is expanded by a linear combination of the pseudo-atomic orbital (LCPAO),

$$\Psi_{\alpha(\beta)}(\mathbf{r},\mathbf{k},\mu) = \sum_i c^{R_n}_{i,\mu,\alpha(\beta)} \phi_i(\mathbf{r}) e^{i\mathbf{R}_n\cdot\mathbf{k}} \tag{2.83}$$

where $R_n$ is the periodic vector of the crystal. By inserting Eq. (2.83) to Eq. (2.82), the spin density matrix now can be written as

$$n(\mathbf{k},\mu) = \begin{pmatrix} n_{\alpha\alpha}(\mathbf{k},\mu) & n_{\alpha\beta}(\mathbf{k},\mu) \\ n_{\beta\alpha}(\mathbf{k},\mu) & n_{\beta\beta}(\mathbf{k},\mu) \end{pmatrix} \tag{2.84}$$

,

where

$$n_{\alpha\beta}(\mathbf{k},\mu) = \sum_{i,j} [c^{R_n *}_{i,\mu,\alpha} c^{R_n}_{i,\mu,\beta} S_{i,j}] e^{i(\mathbf{R}_n\cdot\mathbf{k})}. \tag{2.85}$$

In Eq. (2.85), $S_{i,j}$ is the overlaping matrix.

Finally, the up- and down-spin densities in the $k$-space can be deduced from the $2\times 2$ spin density matrix of Eq. (2.84) by unitary transformation using $U$ matrix of Eq. (2.74). After some algebra, we find that

$$n'_\uparrow = \frac{1}{2}(n_{\alpha\alpha}+n_{\beta\beta}) + \frac{1}{2}(n_{\alpha\alpha}-n_{\beta\beta})\cos\theta + (\mathtt{Re}\ n_{\alpha\beta}\cos\phi - \mathtt{Im}\ n_{\alpha\beta}\sin\phi)\sin\theta \tag{2.86}$$

and

$$n' = \frac{1}{2}(n_{\alpha\alpha}-n_{\beta\beta}) - \frac{1}{2}(n_{\alpha\alpha}-n_{\beta\beta})\cos\theta + (\mathtt{Re}\ n_{\alpha\beta}\cos\phi - \mathtt{Im}\ n_{\alpha\beta}\sin\phi)\sin\theta \tag{2.87}$$

where

$$\phi = -\arctan\left(\frac{\mathtt{Im}\; n_{\alpha\beta}}{\mathtt{Re}\; n_{\alpha\beta}}\right) \tag{2.88}$$

and

$$\theta = \arctan\left(\frac{2(\mathtt{Re}\; n_{\alpha\beta}\cos\phi - \mathtt{Im}\; n_{\alpha\beta}\sin\phi)}{n_{\alpha\alpha} - n_{\beta\beta}}\right). \tag{2.89}$$

Considering the fact that the wave function is given by a linear combination of pseudo atomic orbitals, this spin density matrix can be decomposed into its atomic components.

### 2.4.5 The Berry phase method for the electric polarization calculation

In this study, the SOI is strongly affected by the electric field. Therefore, evaluation of the electric polarization necessary to confirmed the realibility of the results in the present calculations. Here, we apply the Berry phase method for the calculation of electric polarization.

Traditionally, the electric polarization $\mathbf{P}$ can be evaluated by using approximate models such as the Claussiuss-Mosotti models of solids[75]. This is due to the fact that the ionic crystal are represented by the point charge model (PCM). However, considering the fact that the electron density $n(\mathbf{r})$ is a continous function of $\mathbf{r}$, there are no way of finding a unique values of $\mathbf{P}$ as a sum of a dipole units. this problem can be solved by considering the change of polarization, where in quantum mechanics is related to the geometric Berry phase involving integrals over the phases of the electronic wave functions.

Mathematically, the electic polarization $\mathbf{P}$ can be expressed by a sum of dipole units $p_i$ as

$$\mathbf{P} = \sum_{i=1}^{3} P_i \mathbf{R}_i \tag{2.90}$$

where $\mathbf{R}_i$ is ionic position vector. In Eq. (2.90), $P_i$ can be evaluated by using the following Berry phase formula[76, 77].

$$2\pi P_i = \mathbf{G}_i \cdot \mathbf{P} = -\frac{e}{(2\pi)^3} \sum_{\sigma} \int_{\beta} dk^3 \mathbf{G}_i \cdot \left( \frac{\partial}{\partial \mathbf{k'}} \eta_{\sigma}(\mathbf{k}, \mathbf{k'}) \right)_{\mathbf{k}=\mathbf{k'}} \tag{2.91}$$

where $\int_{\beta}$ means that the integral over first Brillouin zone of which volume is $V_B$, and $\eta_{\sigma}(\mathbf{k}, \mathbf{k'})$ is the quantum phase expressed as

$$\eta_{\sigma}(\mathbf{k}, \mathbf{k'}) = \Im \left[ \ln \left( det \left\langle u^{\mathbf{k}}_{\sigma,\mu} | u^{\mathbf{k'}}_{\sigma,\nu} \right\rangle \right) \right] \tag{2.92}$$

where $\mu$ and $\nu$ run over the occupied states. In the OpenMX code, the overlap integral is evaluated in the momentum space, and the expectation value of position operator is evaluated by using the same real space mesh as for the solution of Poisson equation.

# Chapter 3

# Rashba effect on strained ZnO

## 3.1 Introduction

Recently, the effect of spin orbit interaction (SOI) on the spin texrtures attracted much scientific interest because it plays an important role in spintronics device operation. Especially, the Rashba effect [25] attracts much attention since it enables operation of the spin field effect transistor [29]. Here, two dimensional electron gas (2DEG) system is an ideal platform for spintronics because it can be controlled by an external electric field or by strain effect.

ZnO is one of the promising material candidate for spintronics, which is due to the high quality of the two dimensional electron system [50]. Here, for the spintronics applications, clarification of the SOI in ZnO is crucially important. However, strain has significant effect on the electronic structure of ZnO [78]. Therefore, it is is expected that strain induces the new physical properties, which is expected to be useful for spintronics devices.

In this chapter, we present detailed first principle density-functional calculations of strained ZnO. To clarify the effect of SOI, we investigate the spin textures. We find that strain controls SOI in ZnO, where the inversion Rashba spin rotations are observed. We clarifiy that this inversion of Rashba rotation is due to the fact that the strain changes the direction of the electric polarization around the Zn atoms. We also find that the Rashba spin-orbit strength can be effectively controlled by tunning the strain. Finally, the possible applications for the spintronics devices are discussed.

This chapter is organized as follows: Details of the calculation methods are described in Sec. 3.2. In Sec. 3.3 we show the calculated results of the electronics properties of bulk ZnO including the effect of SOI. We also present the calculated results of the electronic properties under influence of the strain effect. Furthermore, a discussion about the possible spintronics devices applications are also presented in the same section. finally, we give conclusion of this chapter in Sec. 3.4.

## 3.2 Computational detailes

We carry out first principle electronic structure calculations based on the density functional theory (DFT) within the generalized gradien approximation [66] by using the OpenMX code [67]. We use norm-conserving pseudo-potentials [68] and the wave functions are expanded by the linear combination of multiple pseudoatomic orbitals (LCPAOs) generated by using a confinement scheme [69, 70]. The orbitals are specified by Zn6.0-$s^2p^2d^2$ and O5.0-$s^2p^2d^1$, which means that the cutoff radii are 6.0 bohr and 5.0 bohr for the Zn and O atoms, respectively, in the confinement scheme [69, 70]. Two primitive orbitals expand $s$, $p$, and $d$ orbitals of the Zn atom and in the case of the O atom, two and one primitive orbitals expand $s$ and $p$ orbitals and $d$ orbitals, respectively. The SOI is included in our fully-relativistic calculation. The 12x12x12 k-point grid is used and geometries are optimized untill the force acting on each atom is less than 0.001 eV/A. To evaluate spin polarization in $k$-space, we calculate the $k$-space spin density matrix using the spinor wave functions, which are calculated by using the OpenMX code[74].

## 3.3 Results and discussion

### 3.3.1 Electronic properties of ZnO

In the most stable structures, ZnO forms wurtzite crystal as shown in Fig. 3.1. The unit vectors of the unit cell are given by

$$\vec{a}_1 = (1/2, \sqrt{3}/2, 0)a \tag{3.1}$$

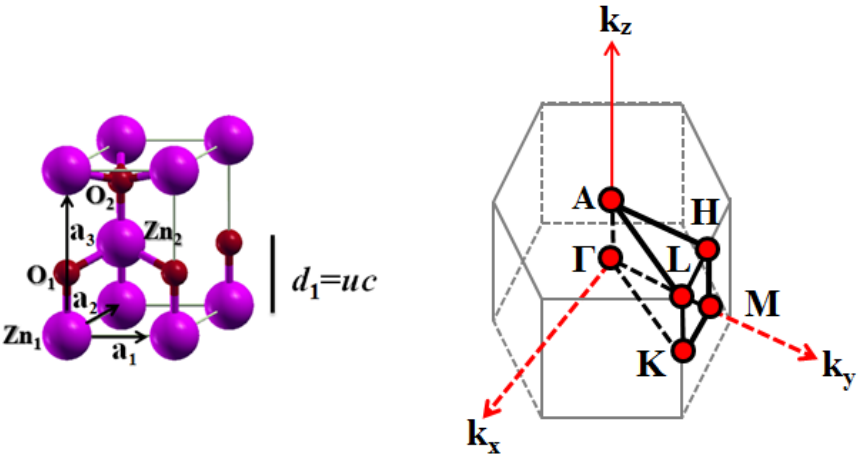


FIGURE 3.1: Crystal structure of wurtzite ZnO and its first Brillouin zone.

$$\vec{a}_2 = (1/2, -\sqrt{3}/2, 0)a \tag{3.2}$$

$$\vec{a}_3 = (0, 0, c/a)a \tag{3.3}$$

where $a$ and $c$ are the lattice constants in the $a$ and $c$-directions, respectively. The Zn atoms are located at $(0, 0, 0)$ and $(2/3, 1/3, 1/2)$ whereas the O atoms are located at $(0, 0, u)$ and $(2/3, 1/3, u + 1/2)$. The length of Zn-O bond along the $c$-axis is given by $d_1 = uc$, where $u$ is the internal parameter.

TABLE 3.1: The optimized lattice parameter, which is compared to those of previous calculation and experimental results.

| Methods | $a_0$ (Å) | $c_0$ (Å) | $c_0/a_0$ | $u_0$ |
|---|---|---|---|---|
| GGA (present work) | 3.284 | 5.303 | 1.615 | 0.379 |
| GGA (ref. [80]) | 3.286 | 5.299 | - | - |
| GGA (ref. [84]) | 3.287 | 5.307 | - | - |
| Exp. (ref. [82]) | 3.253 | 5.204 | 1.602 | 0.382 |

Tabel 3.1 shows the calculated value of the optimized lattice parameters, which is compared to those of previous calculation and experimental results. The calculated values of the optimized lattice constants are $a_0 = 3.284$ Å, and $c_0 = 5.303$ Å. These values are in a good agreement with those of previous GGA calculations ($a_0 = 3.286 - 3.287$ Å and $c_0 = 5.299 - 5.307$ Å) [80, 84]. The present values are slightly larger than the experimental values: $a_0 = 3.253$ Å and $c_0 =$

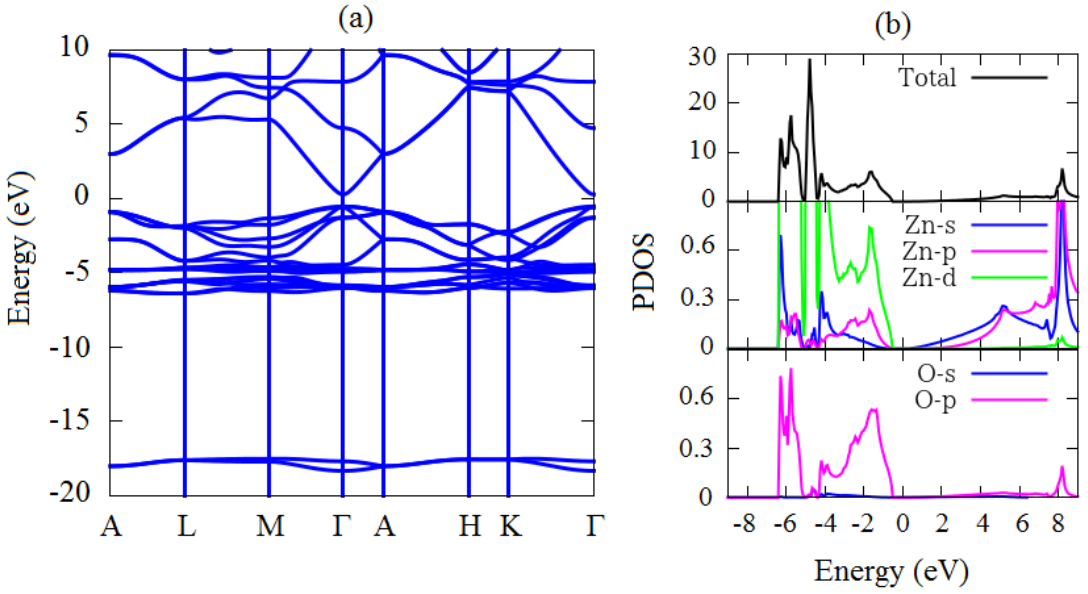


FIGURE 3.2: The electronic structures of ZnO. (a) the Band structures and (b) the density of states projected onto the Zn and O atoms are shown.

5.204 Å[82]. Furthermore, the optimized parameters $c_0/a_0$ and $u_0$ are 1.615 and 0.379, respectively, and slightly different than those of the ideal wurtzite geometry ($c_0/a_0 = 1.633$ and $u_0 = 0.375$) [86]. However, these calculated values are in a good agreement with experimental values ($c_0/a_0 = 1.602$ and $u_0 = 0.382$) [82].

TABLE 3.2: The calculated value of the band gap and energy position of the Zn-*d* orbitals compared with those of previous calculation and experimental results.

| Methods | $E_g$ (eV) | $E_{\mathrm{Zn}-d}$ (eV) |
|---|---|---|
| GGA (present work) | 0.814 | -6.05 |
| GGA (ref. [84]) | 0.814 | - |
| Exp. (ref. [83]) | 3.34 | - |
| GGA (ref. [80]) | - | -5.09 |
| Exp. (ref. [81]) | - | -7.5 |

Figure 3.2(a) shows the calculated results of the electronic band structures of the bulk ZnO. We find that the band structures show a direct band gap, where the conduction band bottom (CBB) and the valence band maximum (VBM) are located on the same high symmetry point, the Γ point. The calculated value of energy gap is found to be 0.814 eV [see table 3.2], which is smaller than those of experimental value (3.34 eV)[83], but this value is consistent with those of past GGA (0.81 eV)[84] calculation.

To clarify the atomic contribution of the electronic band structures, we calculate the partial density of states (PDOS) projected to the Zn and O atoms in the unit cell. As shown in Fig. 3.2(b), we find that the CBB mainly consists of the Zn-$s$ orbitals, whereas the VBM is characterized by the strong hybridization between the O-$p$ and the Zn-$s$ orbitals. The hybridization of $p-d$ orbitals occures in the energy range of 0 to -6.5 eV. The strongest character of the Zn-$d$ orbitals is observed around -6.05 eV [see table 3.2], which is slightly higher than those of the experimental value (-7.5 eV)[81]. However, this value is in good agreement with previous GGA (-5.9 eV) [80] calculation.

### 3.3.2 Rashba effect on ZnO

For the spintronics applications, it is very important to clarify the effect of SOI in ZnO. Here, we performed fully relativistic DFT calculation by including the effect of SOI. In this calculation, our considerations are focused on the CBB since n-type ZnO is really achieved by introducing Mg doping [87]. This is supproted by the fact that the high carrier concentration on the n-type ZnO has been experimentally observed[54].

As shown in Fig. 3.3(a), we find that a very small Rashba spin split bands are observed in the CBB. These splitting linearly depends on the wave vector $k$ at near the $\Gamma$ point [Fig. 3.3(b)]. We also find that the spin-polarized two bands are observed around the $\Gamma$ point, and these two bands are degenerated at the $\Gamma$ point because of the time reversability. In these spin-split bands, we find that the spin textures show the Rashba spin rotations, where their orientations are found to be clockwise and anti-clockwise directions for the upper and the lower bands, respectively [Fig. 3.3(c) and (d)].

To clarfy the origin of the Rashba spin rotations, we consider the SOI in the case of two-dimensional free electron system defined on the ($k_x$-$k_y$) plane. The Hamiltonian described SOI term is expressed by

$$H_{SOI} = \alpha_R(k_y\sigma_x - k_x\sigma_y) \tag{3.4}$$

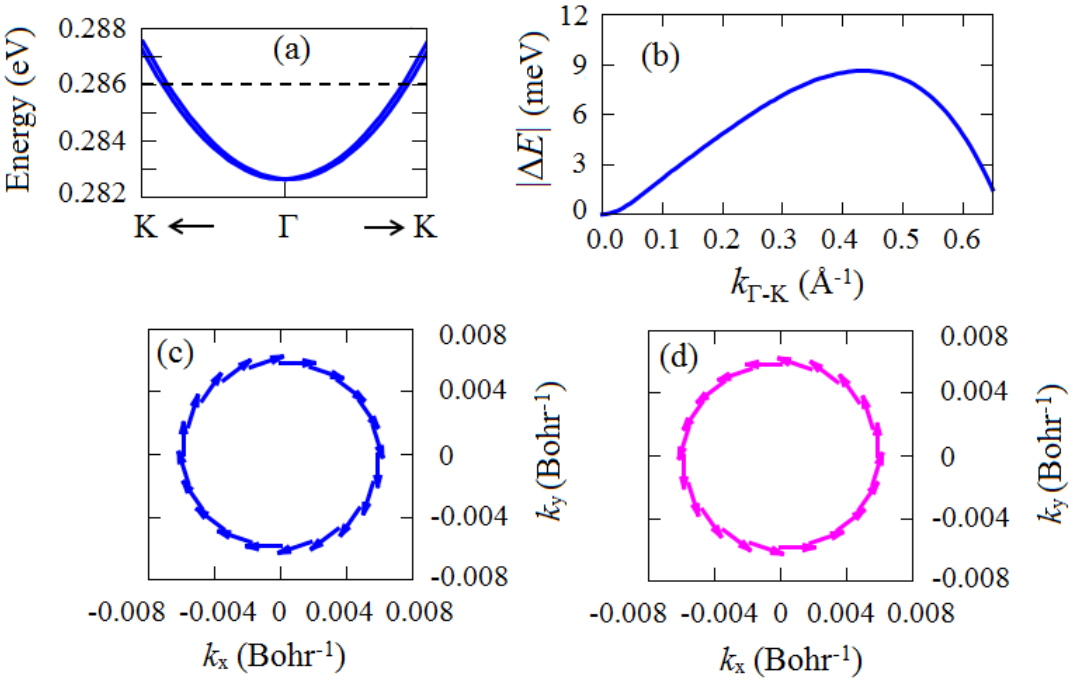


FIGURE 3.3: (a) Rashba band splitting of the conduction band bottom (CBB) in around the Γ point and (b) The energy splitting ($\Delta E$) as a function of the wave vector in the Γ-K direction ($k_{\Gamma-K}$) are shown. The spin textures for (a) the upper and (d) lower bands, which are calculated on 3.5 meV above the degenerate states at CBB, are shown.

where $k_x$ and $k_y$ are wave vectors in the $x$ and $y$ directions, respectively, and $\sigma_x$ and $\sigma_y$ are Pauli matrixes. In this expression, $\alpha_R$ is the Rashba coupling parameter, which is defined by the relation

$$\alpha_R = -e\hbar E_z/4m^2c^2 \tag{3.5}$$

where $E_z$ is the electric field which is perpendicular to the two-dimensional ($k_x$-$k_y$) plane and $m$, $c$, and $e$ are the effective mass, the light velocity, and the elementary charge, respectively.

The Hamiltonian in Eq. (3.4) leads to the fact that the dispersion relation and the spin polarization are expressed by

$$E_\pm = \frac{\hbar^2 k^2}{2m^*} \pm \alpha_R k \tag{3.6}$$

and

$$\mathbf{P}_{\pm} = \left\langle \psi^{\pm} \left| S \right| \psi^{\pm} \right\rangle = \frac{1}{|k|} \begin{pmatrix} \mp k_y \\ \pm k_x \\ 0 \end{pmatrix}, \tag{3.7}$$

respectively, where $m^*$ is the effective electron mass and $S$ is the spin operators which consists of three components, $S_x$, $S_y$, and $S_z$. In Eq. (3.6), the spin-split bands are labelled by the + and - signs for the upper and lower bands, respectively, and their spins lie in the $x-y$ plane and rotate in the opposite directions.

When $E_z < 0$, this leads to the fact that the condition of $\alpha_R > 0$ is obtained. Consequently, due to the Eq. (3.7), the directions of the spin rotation are clockwise and anti-clockwise for the upper and lower bands, respectively. On the other hand, Rashba spin rotation becomes opposite in the case of $E_z > 0$, which is due to the fact that the condition that $\alpha_R < 0$ is achieved. Therefore, we clarified that the Rashba spin rotation are sensitively modified by the direction (sign) of the electric field.

Since the Rashba spin rotations are strongly affected by the electric field, their origin can be further clarified by studiying the electric polarization. To confirmed this, we then study the electric polarization by using point charge model (PCM). Here, the position of the Zn atom are set to be the original point (0,0,0) since the CBB mainly originates from the Zn-$s$ orbitals.

We consider the PCM including $Zn^{2+}$ and $O^{2-}$ ions and evaluate the polarization difference:

$$\Delta\mathbf{P} = \mathbf{P}(c/a, u) - \mathbf{P}(c/a, u_{ideal}) \tag{3.8}$$

where $c/a$ and $u$ are the optimized parameter and $u_{ideal} = 0.375$. We find that the PCM results show the negative value of $\Delta P$, which is -0.0271 C/m$^2$. This value leads to the fact that the condition that $E_z > 0$ is obtained. Therefore, clockwise and anti-clockwise direction of the Rashba spin rotations for the upper and lower bands, respectively, in Fig. 3.3 are well explained based on the PCM.

To confirm the reliability of the above-mentioned PCM, we calculate the electric polarization by using Berry phase (BP) method [76, 77]. We find that the value of $\Delta P$ calculated from the BP method is -0.031 C/m$^2$, which is very close to the

result obtained by using the PCM (-0.0271 C/m$^2$). These values are also in a good agreement with those of past calculations (-0.032 C/m$^2$ to -0.057 C/m$^2$) [88, 89]. This indicates that the calculated results of electric polarization obtained by using the PCM are reliable.

### 3.3.3 The effect of strain

Now, we study the effect of strain on the electronic properties of ZnO. We consider a wide range of biaxial strain (up to $\pm 8\%$) which is perpendicular to the $c$ axis. We define the degree of biaxial strain as

$$\epsilon_{xx} = (a - a_0)/a_0 \tag{3.9}$$

where $a_0$ is the unstrained lattice constant. In this case, we fix the lattice constant $a$ at certain strain condition, while the lattice constant $c$ and internal parameter $u$ are allowed to relax. We study two different cases, i.e, the tensile biaxial strain (TBS) which increases the lattice constant $a$ and the compressive biaxial strain (CBS) which decreases $a$ [Fig. 3.4(a)]. This strain can be achieved by using impurity doping [90] and/or introducing lattice mismatch between ZnO and substrate [91]. In fact, several experimental studies confirmed that the CBS can be achieved using ZnO epilayer grown on sapphire substrate [91]. Meanwhile, the TBS can be achieved by applying impurity doping such as Mg and Co doping [87, 90].

Fig. 3.4(b) shows the calculated results of the optimized structural parameter of the strained system. We find that under TBS, the value of $c/a$ decreases, but the value of $u$ increases. These results indicate that the bondlength between the Zn and O atoms in the $c$-direction ($d_1$) enhances, while other bondlength in the other orientations ($d_2 = d_3 = d_4$) reduces [see the insert of Fig. 3.4]. However, opposite trend of structural parameter is observed in the case of CBS. Here, increasing and decreasing trends of $c/a$ and $u$, respectively, are observed resulting that the bondlength $d_1$ and $d_2 = d_3 = d_4$ reduces and enhances, respectively. Therefore, we conclude that the structural parameter is sensitively affected by the strain.

Since the strain strongly influences the structural partameters of ZnO, we expect that it also strongly modify the electronic properties. To confirmed this, we calculate the band structures of the strained system, where the calculated result is

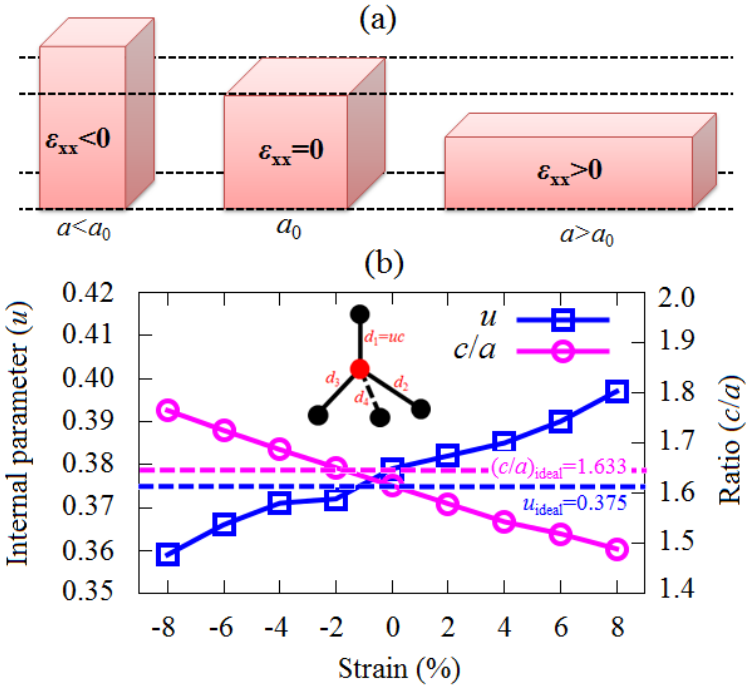


FIGURE 3.4: (a) Schematic view of biaxial strain. The biaxial strain is defined by the changing in-plane lattice constant $a$ in the two different ways, i.e. tensile biaxial strain (right side) and compressive biaxial strain (left side). (b) Optimized structural parameter ($c/a$,$u$) as a function of biaxial strain. The insert shows the thetrahedrally coordiated atoms in the unit cell. $d_1$ represents the bondlength between the Zn and O atoms in the $c$- direction, while $d_2 = d_3 = d_4$ define the bondlength of the Zn and O atoms in the non-polar directions.

shown in Figure 3.5. We find that the band structures of strained system show a direct band gap, which is similiar to those of the unstrained system. However, the position of conduction band bottom (CBB) and valence band maximum (VBM) shift under different strain condition. For the case of TBS, the CBB and VBM shift to be lower and higher energy than those of unstrained system, respectively. On the other hand, these shifting energy becomes opposite in the case of CBS, indicating that strain sensitively changes the band gap. We find that the substantial values of energy gap decreses for the case of TBS ($E_{g-\epsilon_{xx}=4\%}$ = 0.731 eV), wherease it enhances in the case of CBS ($E_{g-\epsilon_{xx}=-4\%}$ = 0.86 eV) compared to those of the unstrained system ($E_{g-\epsilon_{xx}=0\%}$ = 0.814 eV). It is therefore concluded that the electronic properties of ZnO is significantly modified by the strain.

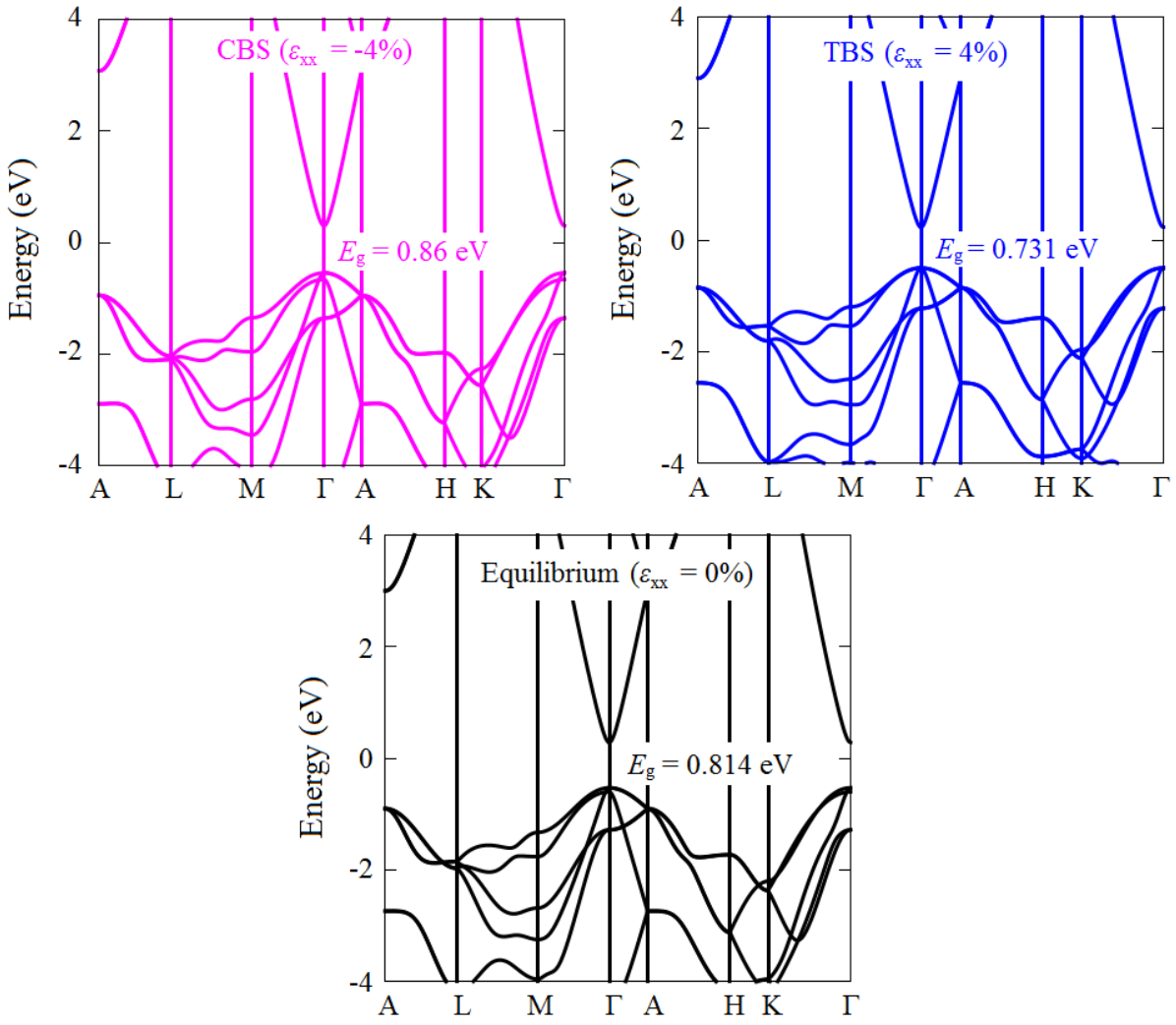


FIGURE 3.5: The band structures of ZnO under different strain condition. The black, blue, and the pink lines represent the band structures of the unstrained, TBS (4%), and CBS (-4%), respectively.

### 3.3.4 Tunable Rashba effect by strain

As mentioned before that the strain has significant effect to the electronic structures of ZnO. In this case, the new physical properties is expected to be observed when the SOI is taken into account. Especially the Rashba effect, which is important for spintronics devices, is expected to be affected by introducing strain. Therefore, clarification of the Rashba effect on the strained system is crussially important.

Figure 3.6 shows the result of the strain effect on the spin-split bands at CBB and the spin textures. We find that, the Rashba band splitting substantially enhances under increasing of the strain. In the case of TBS, the spin textures show the

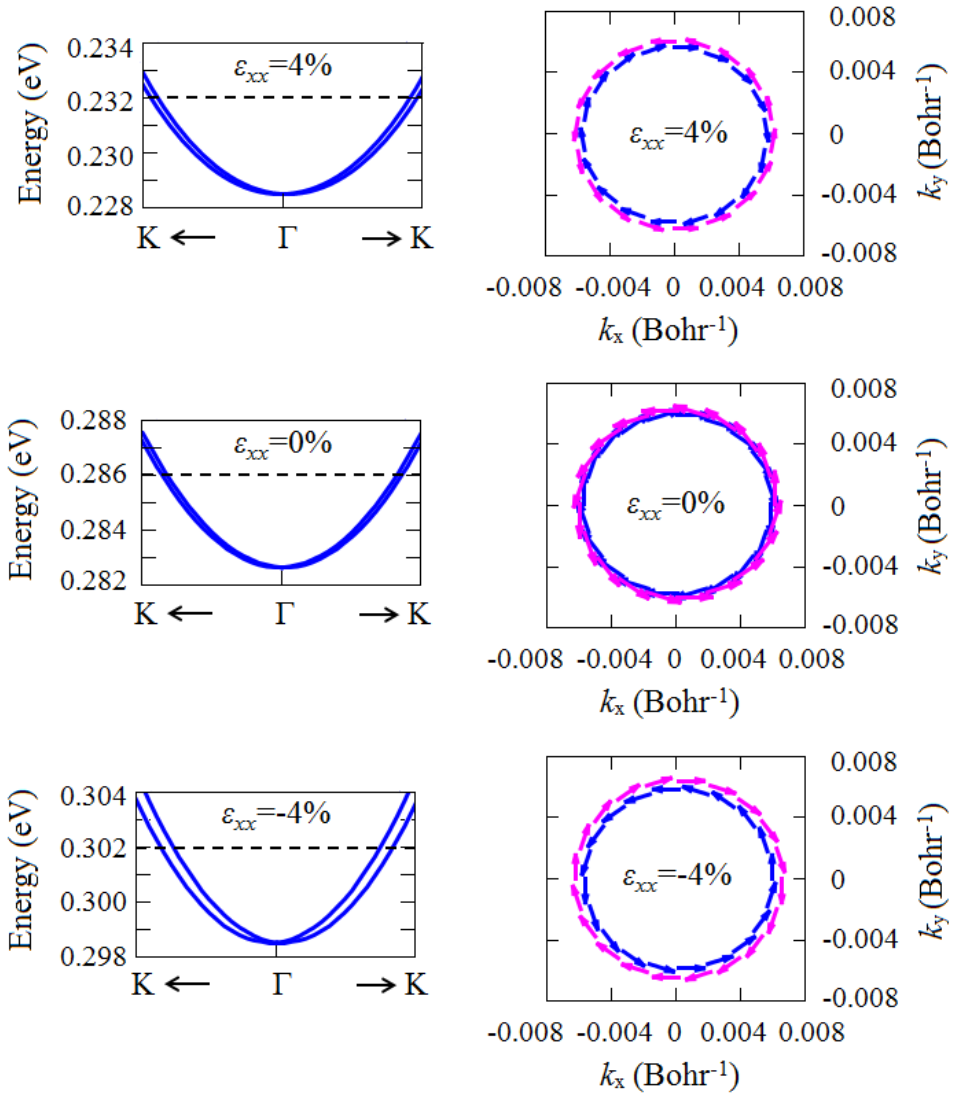


FIGURE 3.6: The band splitting and the spin textures for different strain condition. The spin textures are calculated on 3.5 meV above the degenerate states of at the CBB.

Rashba spin rotation, which has the same direction as those for the unstrained system. On the contary, the directions of the Rashba spin rotations becomes opposite in the case of CBS, indicating that the Rashba spin rotations can be inversed by applying biaxial strain.

Considering the fact that the Rashba spin rotation is strongly affected by the sign (direction) of the electric field as mentioned before, we expect that the negative and positive electric fields $E_z$ are introduced under the CBS and TBS, respectively. To clarify this, we performed the PCM to calculate the electric polarization in the strained ZnO. Under substantial CBS, where $u < u_{ideal}$ [Fig. 3.7(a)], the PCM leads to the positive $\Delta P$ [Fig. 3.7(b)]. This positive value of $\Delta P$ is expected to

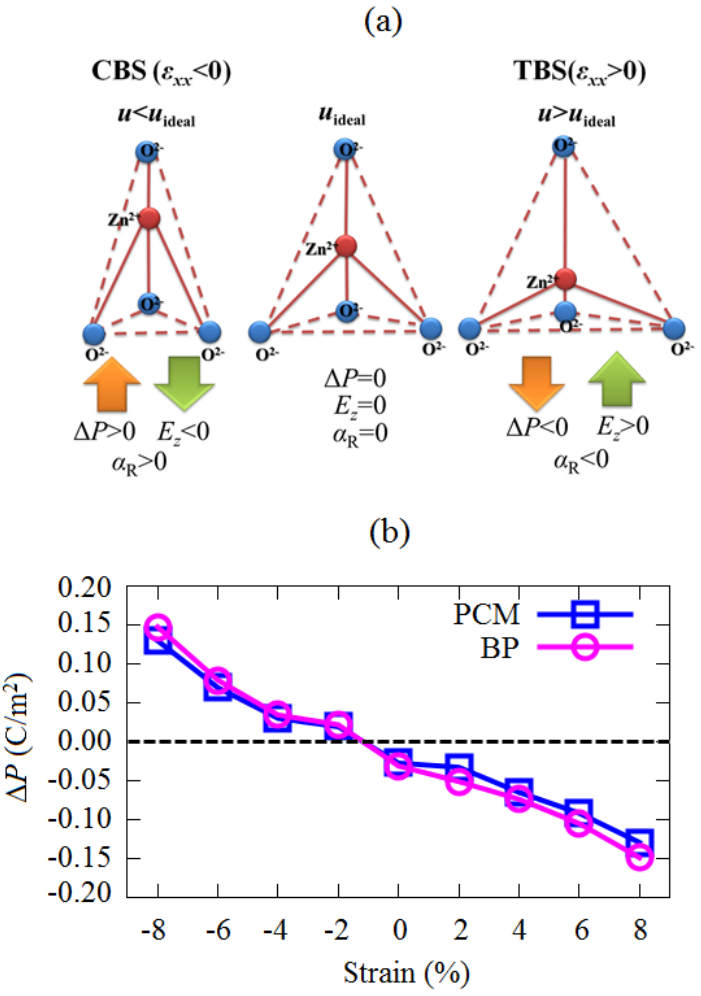


FIGURE 3.7: (a) Schematic view of the strain and the Rashba parameter. (b) Electric polarization difference $\Delta P$, which is calculated by using the Berry phase (BP) method and point charge model (PCM).

induce the fact that $E_z < 0$. On the contrary, substantial TBS leads to the fact that $u > u_{ideal}$. As a result, the negative $\Delta P$ and positive $E_z$ are induced. We therefore conclude that the negative and positive $E_z$ are introduced under CBS and TBS, respectively, and that the directions of the Rashba spin rotations in Fig. 3.5 are consistent with the result of the PCM.

To confirm the reliability of the PCM results, we also calculate the electric polarization by using Berry phase (BP) method [76, 77]. We find that, the PCM results of $\Delta P$ in the strained system are close to those calculated from the BP method [Fig. 3.7(b)]. This indicates that the PCM calculation for the strained system is reasonable.

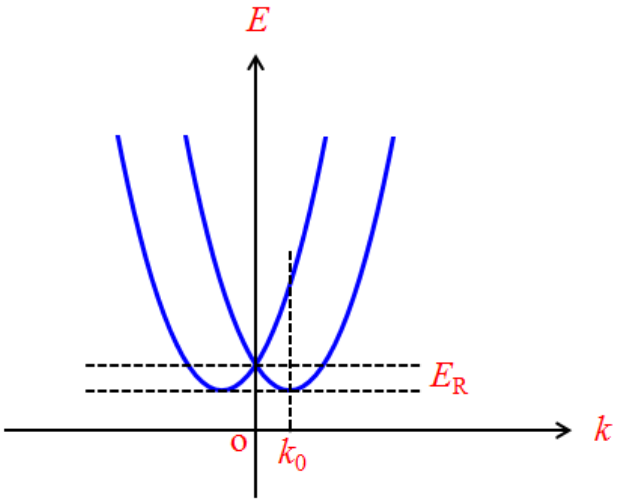


FIGURE 3.8: Schematic view of the parabolic band dispersion and its properties is shown.

### 3.3.5 Discussion

We have clarified that the Rashba spin rotation can be controlled by introducing biaxial strain. This indicates that the Rashba spin-orbit strengths $\alpha_R$ can be effectively tuned by applying strain. Here, we estimated the absolut value of $\alpha_R$ by using the band dispersions in Fig. 3.6.

According to the Eq. (3.6), it is revealed that the band dispersion is characterized by the parabolic profile. This indicate that the Rashba spin-orbit strength $\alpha_R$ can be evaluated directly from the properties of parabolic band dispersion, which is schematically shown in Fig. 3.8. We can see that two spin polarized band dispersions cross at $k = 0$, while they have energy extremum at $k = \pm k_0$, where $k_0$ is the momentum off-set. At $k = k_0$, this energy band extremum can be expressed as

$$E_R = \frac{\hbar^2 k_0^2}{2m^*} + \alpha_R k_0 \tag{3.10}$$

where $E_R$ is the Rashba energy which is defined as the energy of the band extremum with respect to the energy $E_0$ for which the band cross at $k = 0$. At the same time, the gradient energy band dispersion vanishes at $k = k_0$, which leads to the relation

$$m^* = -\frac{\hbar^2 k_0}{\alpha_R}. \tag{3.11}$$

By inserting Eq. 3.11 to Eq. 3.10, we obtain the equation for $\alpha_R$:

$$\alpha_R = \frac{2E_R}{k_0}. \tag{3.12}$$

Now, we can evaluate the Rashba spin-orbit strength $\alpha_R$ directly by using Eq. (3.12).

Figure 3.9(a) shows the calculated results of the strain dependence of $k_0$, $E_R$, and $\alpha_R$. We find that the absolute values of $\alpha_R$ increases when strain is applied [Fig. 3.9 (c)]. We also find that introducing strain enhances the values of $k_0$ and $E_R$ [Fig. 3.9 (a) and (b)]. Considering the fact that strain induces the enhancement of the magnitude of the electric polarization, the absolute value of $\alpha_R$ increases, which is consistent with the SOI on the two dimensional free electron model. Since the opposite direction of electric fields is identified on both of TBS and CBS, it is expected that their values of $\alpha_R$ have the opposite signs. For example, the calculated values of $\alpha_R$ is 4.41 meVÅ in the case of $\epsilon_{xx} = -4\%$, whereas it is -2.19 meVÅ for the case of $\epsilon_{xx} = 4\%$. Therefore, we clarified that the substantial values of $\alpha_R$ can be effectively tuned by applying biaxial strain.

Next, we discuss the possible spintronics applications of ZnO. Recently, the quantum well structure of ZnO has been extensively studied [92, 93]. Our calculations indicate that two quantum wells consisting of n-type ZnO having opposite directions of the Rashba spin rotations can be realized. By using two quantum wells separated by an energy barrier, an effective spin-filtering due to tunneling is expected to be achieved. In fact, for the spin-filtering device proposed by Koga et.al, two quantum wells having the opposite directions of the Rashba spin rotations were used [95]. Their proposal may give some hint for the device applications of the reversible Rashba effect on ZnO.

Here we discuss another possible application of strained ZnO. We find that the Rashba splitting for the unstrained system is small (the absolute values of $\alpha_R$= 1.15 meVÅ), which is consistent with the observed long spin relaxation time [53, 54]. In fact, a very small Rashba effect on MgZnO/ZnO interface ($\alpha_R$ is 0.70 meVÅ) has been experimentally observed [54]. It is expected that the zero (or very small) Rashba splitting can be achieved when we introduce suitable small biaxial strain.

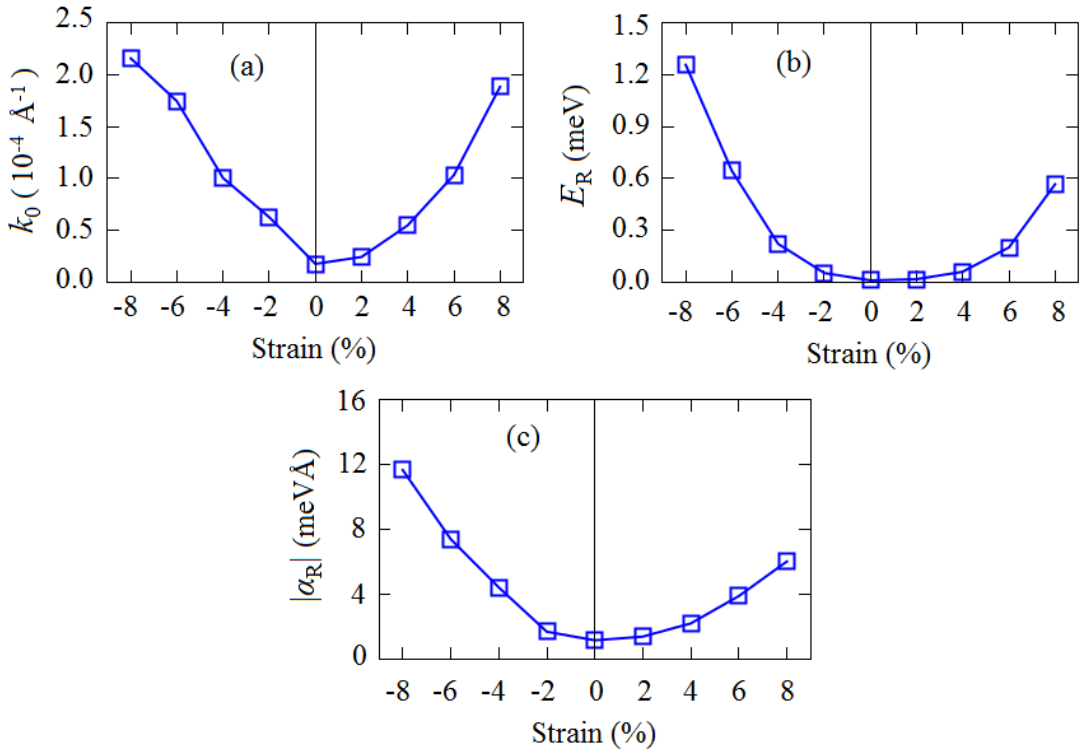


FIGURE 3.9: (a) Momentum off-set $k_0$, (b) Rashba eneregy ($E_R$), and the absolut value of the Rashba parameter ($\alpha_R$) as a function of strain are shown.

When the Rashba effect on ZnO is extremely small, we can achieve a very long spin coherence. Then, ZnO can be used as an effecient spintronics devices.

## 3.4 Conclusion

The effect of SOI on the strained bulk ZnO has been sistematically studied by using first-principles DFT calculations. We found that strain controls the SOI in ZnO, where the inversion Rashba spin rotations are observed between tensile and compressive biaxial strain. We also found that the Rashba spin-orbit strength can be effectively controlled by tuning the strain. Our finding of the inversion Rashba rotation may give some hint for the application of the future spintronisc devices.

According to our finding, the presently used calculation scheme is expected to be useful tools to investigate the Rashba effect on the SOI system materials. Here, a special attention is given to the system having large internal electric field such as oxide interface system materials. Recently, the interface system such as

MgZnO/ZnO were extensively studied [54]. Our study clarified that the effect of strain on interfaces plays an important role in SOI.

Therefore, we conclude that the present system is suitable for spintronics applications.

# Chapter 4

# Persistent Spin helix on the wurtzite ZnO $(10\bar{1}0)$ surface

## 4.1 Introduction

Recently, semiconductor materials having the long spin life time attracted much scientific interests because they achieve an efficient energy saving for spintronics devices. The strongly enhanced spin relaxation time is predicted to be achieved by using persistent spin helix (PSH) materials [32–39]. Theoretical studies predicted that the PSH materials can be realized by using [001]-oriented quantum well (QW) in which the Rashba and Dresselhauss terms are equal; or by using [110]-oriented QW, which is affected by only the Dresselhauss effect[32]. In both cases, the spin-orbit coupling depends linearly on the electron momentum in spesific directions and quasi-one-dimensional orientation of the spin textures is generated[32]. The PSH states has been observed recently for [001]-oriented GaAs/AlGaAs QW [33, 34, 38] and InAlAs/InGaAs QW [35, 37]. Furthermore, the PSH states were also observed for [110]-oriented GaAs/AlGaAs QW, which showed a uni-directional out-of-plane spin directions[39].

The PSH has been widely studied only for the zinc-blende semiconductors. Wurtzite structure semiconductors are promising candidates since the high quality of the two dimensional systems has been experimentally observed [97, 98] and their spintronics application has been discussed [94]. Therefore, achievement of PSH for these semiconductors is expected to be useful.

In this chapter, through first-principles density-functional calculation, we show that the PSH is realized by using the wurtzite ZnO $(10\bar{1}0)$ surface, exhibiting a quasi-one dimensional orientation of the spin textures. We clarify the origin of the spin textures by using the simplified Hamiltonian based on the group theory. Finally, we revealed that the wavelength of the PSH is small compared with those observed for various zinc-blende quantum well structures, indicating that the ZnO $(10\bar{1}0)$ surface is suitable for spintronics applications.

This chapter is organized as follows: Details and calculation methods is given in Sec. 4.2. In Sec 4.3, we present the calculation results including the structural and electronic properties of ZnO $(10\bar{1}0)$ surface and the effect of SOI. Here, the band splitting and the spin textures are presented. We also give clarification about the origin of the spin textures by evaluating the group theory and performing the calculation of the electric polarization. Furthermore, in Sec. 4.4, we give a discussion about our calculated results of the spin-orbit strength and the wavelength, which is compared to the recent experimental results observed on the zinc-blende quantum well structures. Finally, we give some conclussion, which is presented in Sec. 4.5.

## 4.2 Computational detailes

As shown in Chapter 2 that the wurtzite ZnO forms a hexagonal close-packed lattice where the in-plane and axial lattice parameters are represented by $a$ and $c$, respectively. To describe non-polar $[10\bar{1}0]$ surfaces, we here introduce new unit vectors [Fig. 4.1 (a)], which are

$$\vec{a}_1 = (1, 0, 0)a \tag{4.1}$$

$$\vec{a}_2 = (0, c/a, 0)a \tag{4.2}$$

$$\vec{a}_3 = (0, 0, \sqrt{3})a \tag{4.3}$$

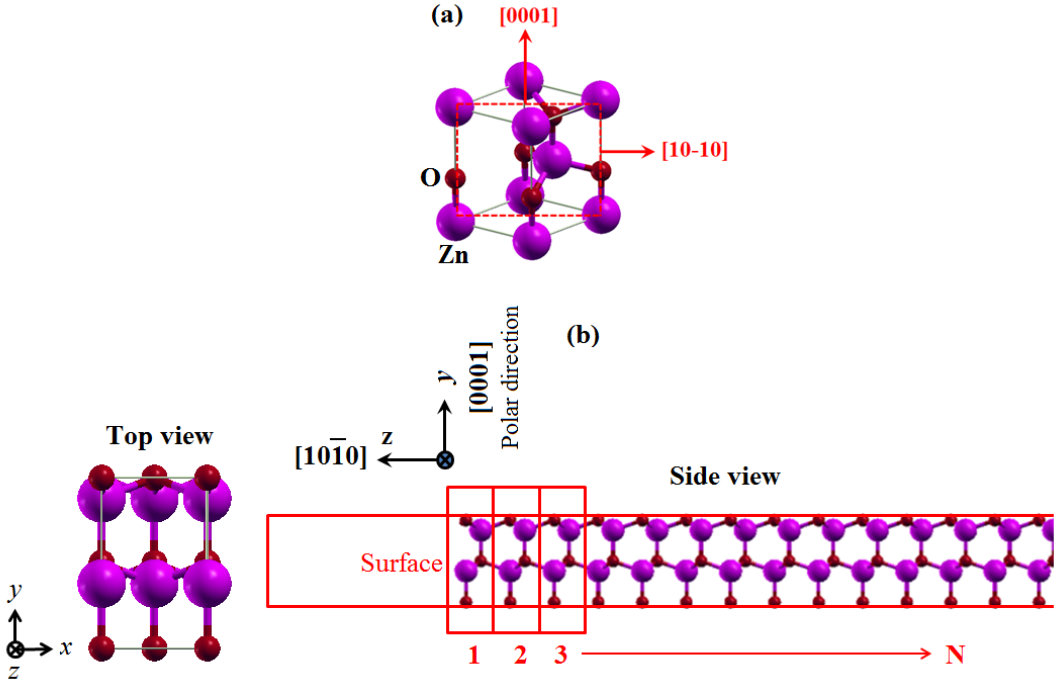


FIGURE 4.1: (a) The unit cell of the bulk ZnO. The [10$\bar{1}$0] and [0001] directions are indicated by the arrow. (b) Top and side views of the slab model of ZnO 10$\bar{1}$0 surface. The polar direction [0001] is set to be the y directions. The number $N$ = 1,2,...$N$ indicates the number of bilayer.

In this new vectors, the unit cell consists of eight atoms. In the new unit vectors, the polar [0001] and non-polar [10$\bar{1}$0] directions are set to be the $y$ and the $z$ directions, respectively [Fig. 4.1 (b)]. Our calculations of the optimized lattice constants show that $a$ = 3.2845 Å, $c$ = 5.3029 Å, $c/a$ = 0.6151, and $u$ = 0.3791. These values are consistent with our previous results[94]. The surface calculations are carried out by using the slab model, which consists of 20-bilayers, and is terminated by hydrogen atoms on the backside [Fig. 4.1(b)]. The vacuum length is over 15 Å to avoid the interactions between the neighboring slabs.

We carry out first-principles electronic-structure calculations based on the DFT within the generalized gradient approximation (GGA)[66] by using the OpenMX code [67]. Here, the 4×6 k-point grid is used and geometries are fully relaxed untill the force acting on each atom is less than 0.001 eV/Å. In our calculation, norm-conserving pseudo-potentials [68] are used. The wave functions are expanded by the linear combination of multiple pseudo-atomic orbitals (LCPAOs) generated by using a confinement scheme [69, 70]. The orbitals are specified by Zn6.0-$s^2p^2d^2$, O5.0-$s^2p^2d^1$, and H5.0-$s^2p^1$: for example, in the case of Zn atom, Zn6.0-$s^2p^2d^2$ means that the cutoff radius is 6.0 bohr in the confinement scheme [69, 70], and

two primitive orbitals for each of $s$, $p$, and $d$ components are used. The SOC is included in our fully-relativistic calculations and the spin textures in $k$-space are calculated by using the $k$-space spin density matrix of the spinor wave functions [74].

## 4.3 Results

### 4.3.1 Structural and electronic properties of ZnO $(10\bar{1}0)$ surface

TABLE 4.1: The atomic relaxation at the uppermost surface in the out-of-plane ($y$) and in-plane ($z$) direction.

| Methods | $\delta_z$(Zn) (Å) | $\delta_y$(Zn) (Å) | $\delta_z$(O) (Å) | $\delta_y$(O) (Å) |
|---|---|---|---|---|
| GGA (present work) | -0.28 | 0.19 | -0.035 | -0.03 |
| LDA (ref. [100]) | -0.36 | - | -0.04 | - |
| LDA (ref. [101]) | -0.32 | - | -0.04 | - |
| B3LYP (ref. [102]) | -0.21 | 0.116 | 0.002 | -0.024 |
| LEED Exp. (ref. [99]) | -0.45 | - | -0.05 | - |

Firstly, we employ DFT calculations to investigate the structural properties of ZnO $(10\bar{1}0)$ surface. Tabel 4.1 shows the calculated result of the atomic relaxation for the top most surface. Calculations for a ZnO $(10\bar{1}0)$ surface identified that the out-of-plane relaxation of Zn and O atoms are $\delta_z(\mathtt{Zn}) = -0.28$ Å and $\delta_z(\mathtt{O}) = -0.035$ Å, respectively [Fig. 4.1(c)]. These values are slightly smaller than previous experimental values of $\delta_z(\mathtt{Zn}) = -0.45$ Å and $\delta_z(\mathtt{O}) = -0.05$ Å [99], but are in a good agreement with past calculations [-0.36 to -0.21 Å ($\delta_z(\mathtt{Zn})$) and -0.04 Å ($\delta_z(\mathtt{O})$)] [100–102]. On the other hand, the in-plane relaxations of Zn and O atoms, $\delta_y(\mathtt{Zn}) = 0.19$ Å and $\delta_y(\mathtt{O}) = -0.03$ Å, respectively, are close to prior calculations [$\delta_y(\mathtt{Zn}) = 0.116$ Å and $\delta_y(\mathtt{O}) = -0.024$ Å] [102].

Next, we study the elctronic properties of ZnO $(10\bar{1}0)$ surface. We investigate the electronic band structures of ZnO $(10\bar{1}0)$ surface in the several high symmetry points of the entire surface Brillouin zone [Fig. 4.2(a)]. As shown in Figure 4.2 (b), the band structures show the normal insulator, where the band gap is observed in the $\overline{\Gamma}$ point. We find that the calculated value of energy gap is 0.902 eV, which is slightly larger than that of bulk system (0.814 eV). Another interesting feature of

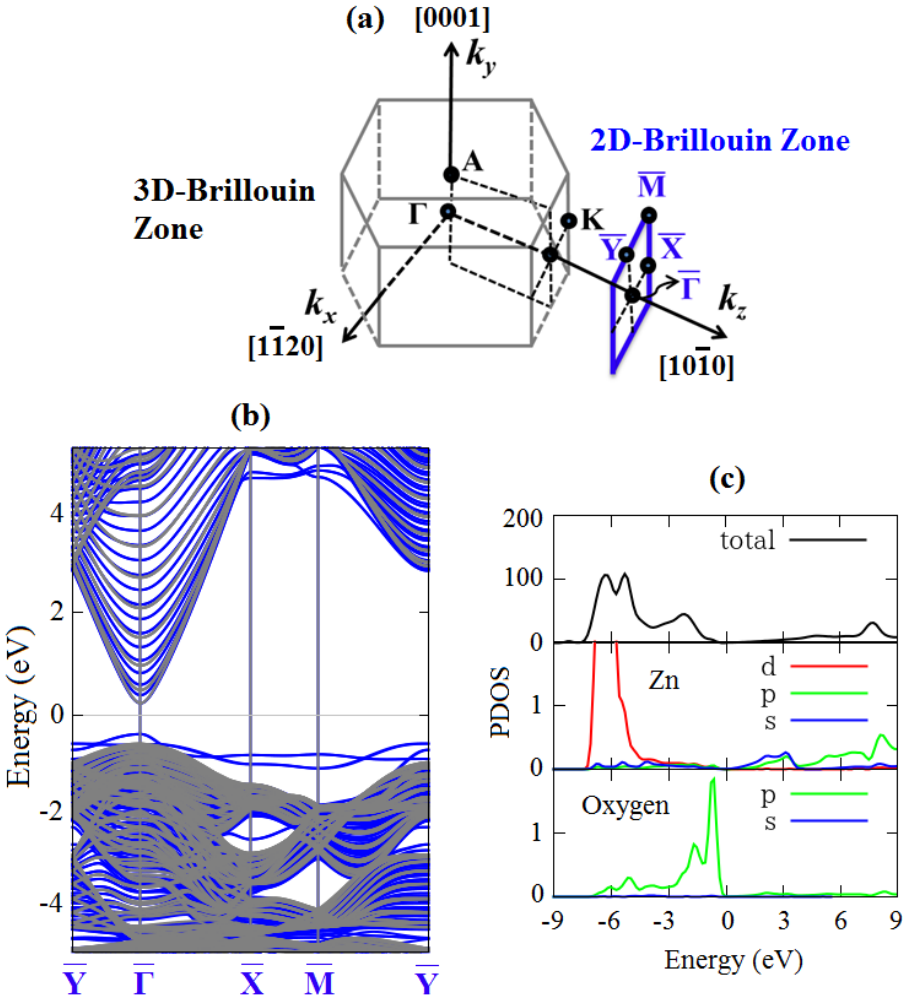


FIGURE 4.2: (a) Brillouin zone of bulk (black lines) and surface systems (blue lines). (b) The band structure of ZnO (10$\bar{1}$0) surface (blue lines) projected to those of the bulk system (black lines) are shown. (b) The calculated result of the partial density of states projected onto the surface atoms.

the band structures is the appearence of the surface states. Here, we find occupied surface states, which is observed in the energy range of -1.3 to -0.65 eV. At $\overline{\Gamma}$ point, occupied surface states are located in the band gap, whereas unoccupied state is resonant with the bulk conduction band bottom (CBB).

To clarify the atomic contribution of the surface-states bands, we performed calculation of the partial density of states (PDOS) projected onto the surface atoms. As shown in Figure 4.2(c), we find that the occupied surface states are characetrized by O-2$p$ orbitals, which is consistent with the results of past calculations using a local density approximation (LDA) [101]. Therefore, we clarified that the O-2$p$ dangling bond states plays an important role in the surface.

Since the surface states are occupied, it is expected that p-type system is achieved by introducing doping effect. Interestingly, several studies confirmed that non-polar wurtzite ZnO film is favorable to produce the p-type systems[103, 104]. The weak p-type conductivity in undoped non-polar film grown on m-plane and r-plane sapphires is observed[104]. Furthermore, p-type conductivity of Na-doped ZnMgO/ZnO nonpolar heterostructures with a carrier concentration of about $3.5\times10^{16}$ $Cm^{-3}$ is achieved [103]. Therefore, the realization of the p-type wurtzite ZnO ( $10\bar{1}0$ ) surface is plausible.

### 4.3.2 The effect of spin-orbit interaction (SOI)

#### 4.3.2.1 Band splitting and the spin textures

Since the surface states appear in the band structures, we expect that they are strongly affected by the SOI. To confirmed this we performed fully relativistic DFT calculation by employing the effect of SOI. Here, the effect of SOI is focused on the occupied surface states in the highest valence band maximum (VBM) along $\overline{Y}$-$\overline{\Gamma}$-$\overline{X}$ symmetry lines. As shown in Figure 4.3, we find that the spin-split bands are observed in the VBM. In the highest occupied surface states, we find that the band splitting is small in the $\overline{\Gamma}$-$\overline{Y}$ direction, whereas it is subtantially large in the $\overline{\Gamma}$-$\overline{X}$ direction, indicating that the band splitting is strongly anisotropic.

We then study the spin textures of the spin-split surface states bands of the highest VBM. We calculate the spin textures projected to the $k_x$-$k_y$ plane in the surface brillouin zone [Fig. 4.4 (a)]. We find that the spin textures of the surface states show quasi-one dimensional orientation in the in-plane $y$ direction [Fig. 4.4(a)]. These spin textures also have the out-of-plane $z$ components [Fig. 4.4(b)]. These quasi-one dimensional spin textures are expected to generate the pointing currents in the direction which is perpendicular to the spin orientation, and induce strongly enhanced spin relaxation time through the PSH mechanism [32]. In fact, a similiar PSH has been predicted on the [110]-oriented zinc-blende QW having the out-of-plane spin orientations [39].

Since our calculation of the spin textures are performed in the surface state bands, we expect that these spin textures are strongly localized. To confirmed this, we study the spatial distribution of spin textures projected to the each atoms in the

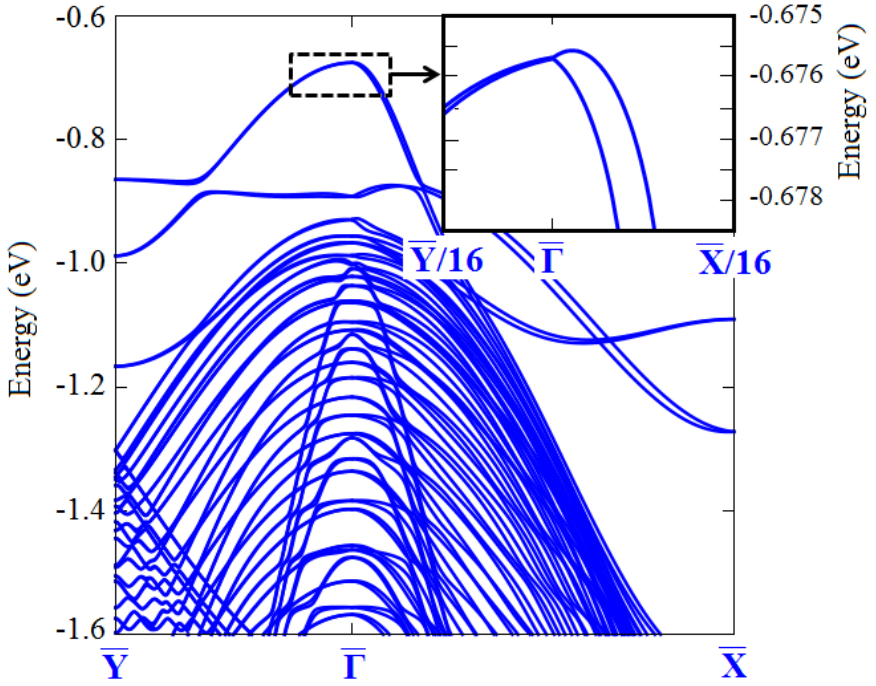


FIGURE 4.3: Band structures near the VBM in the $\overline{Y}$-$\overline{\Gamma}$-$\overline{X}$ symmetry lines. The insert shows the spin-split surface-state bands.

each bilayer. We evaluate bilayer dependent of the spin textures by calculating the expected value of spin by using the relation:

$$\langle S \rangle_{i,\vec{k}} = \sqrt{(S_x)^2_{i,\vec{k}} + (S_y)^2_{i,\vec{k}} + (S_z)^2_{i,\vec{k}}} \tag{4.4}$$

where $i$ is the bilayer index and $\vec{k}$ is the wave vector defined as $k = \sqrt{{k_x}^2 + {k_y}^2}$.

As shown in Figure 4.5, it is revealed that the spin states are strongly localized on the surface region, which is more than 80 percent distributed on the first two bilayers. We find that the localized-spin surface-states mainly originates from the contribution of the O atoms, which is consistent with the previous analyses of the PDOS, where the O-2$p$ dangling bond states play an important role.

#### 4.3.2.2 Group theoretical analyses

To clarify the origin of the spin-split surface states band and spin textures, we consider the SOI based on the group theory [105–108]. Figure 4.6 shows the top and side views of the mirror symmetry projected to the slab model of the ZnO $(10\bar{1}0)$ surface. Here, we observed only one mirror symmetry $M$, which is located

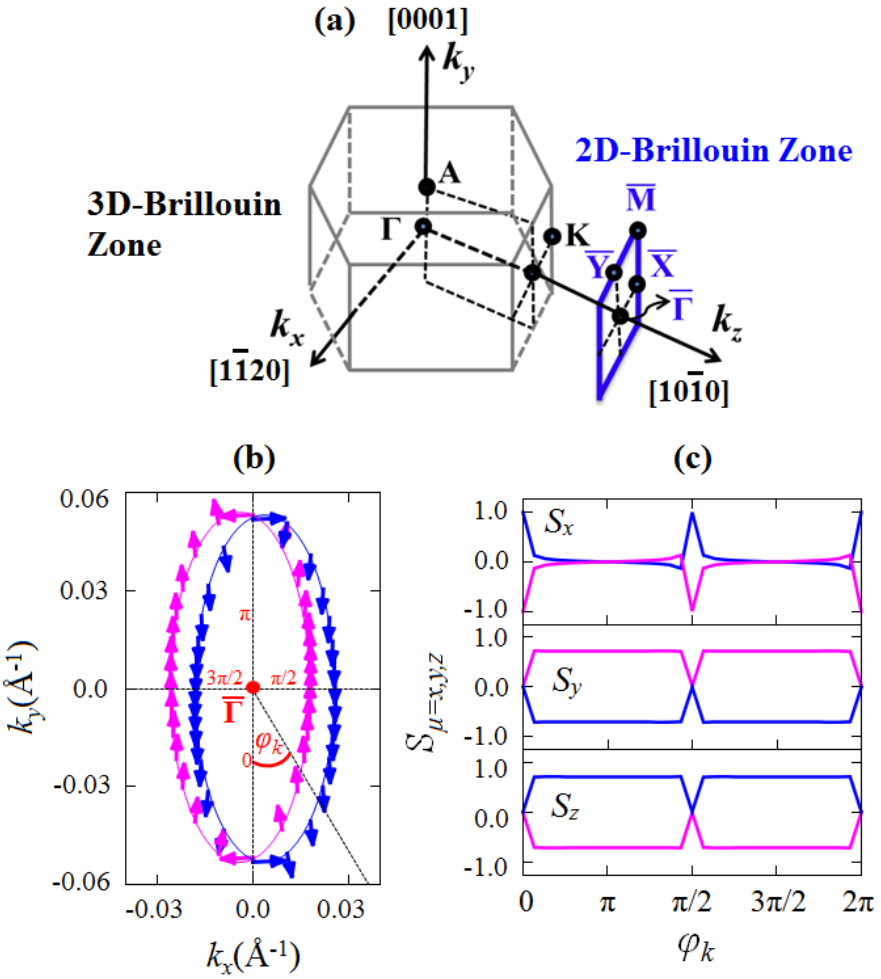


FIGURE 4.4: (a) The brillouin zone of bulk (black lines) and surface (blue lines) systems. (b) The spin textures of the surface state at VBM. The band energy of the spin textures is 1 meV below the highest energy of the occupied surface state. The arrows represent the spin directions projected to the $k_x$-$k_y$ plane. (b) Relationships between rotation angle ($\varphi_k$) and spin components.

on the $y-z$ plane. Due this mirror symmetry $M$, the ZnO (10$\bar{1}$0) surface belongs to the symmetry point group $C_s$. In this case, the mirror reflection operation $M$ transforms $(x, y, z)$ to $(-x, y, z)$. This leads to the fact that the polar ($k_x$, $k_y$, $k_z$) and axial ($\sigma_x$, $\sigma_y$, $\sigma_z$) vectors can be transformed into the new polar and axial vectors, respectively, as given in Tabel 4.2.

The SOI Hamiltonian can be constructed by using all of the possible product between axial and polar vectors. Considering the fact that the SOI Hamiltonian is totally symmetric in the $C_s$ symmetry and including the first-order terms over the wave vectors, the SOI can be expressed by an effective Hamiltonian,

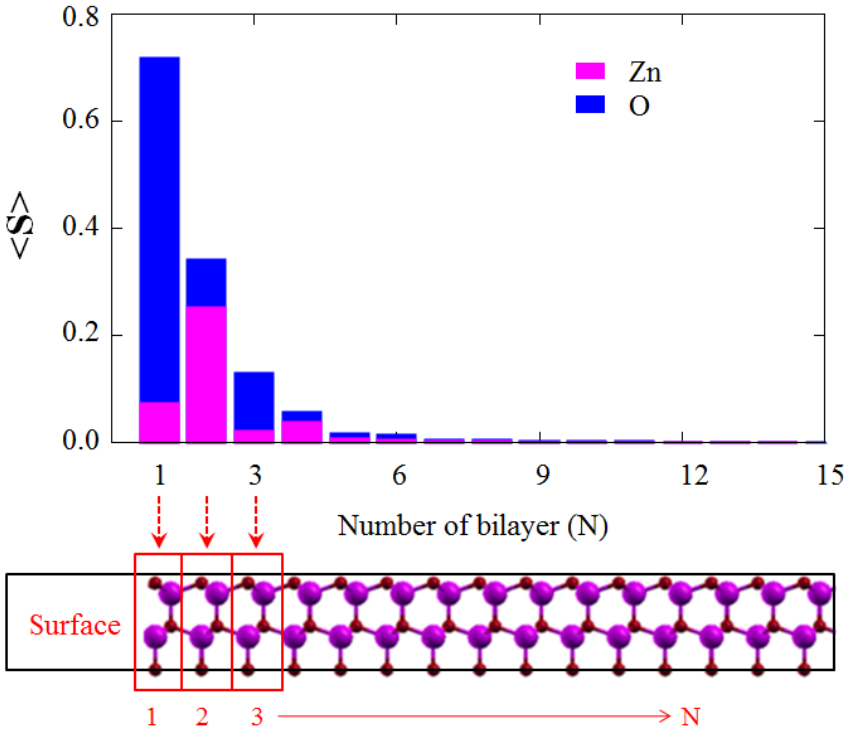


FIGURE 4.5: Expected values of spin projected to the atoms in each bilayer. The calculations are performed for the spin textures of surface states in Fig. 4.4. The top surface is represented by N=1.

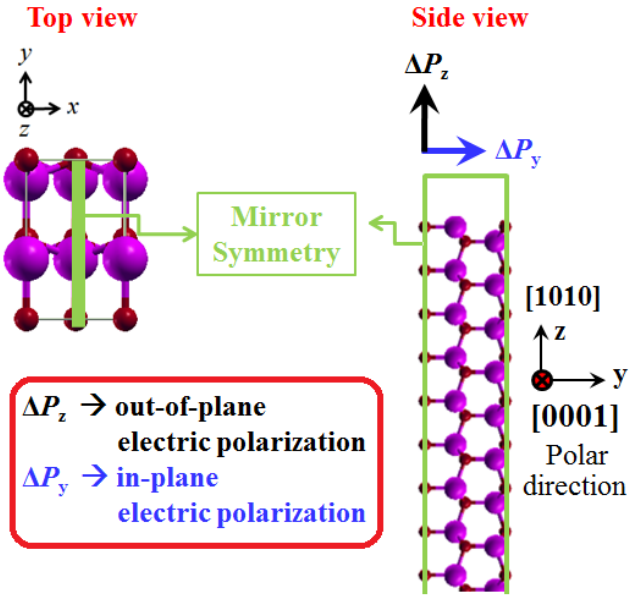


FIGURE 4.6: Mirror symmetry of the surface, which is seen from the top and side views. Only one mirror symmetry ($y-z$ plane) is observed in The ZnO $(10\bar{1}0)$ surface.

TABLE 4.2: Transformation of the polar ($k_x$, $k_y$, $k_z$) and axial vector ($\sigma_x$, $\sigma_y$, $\sigma_z$) in the symmetry point group $C_s$.

| $(x, y, z)$ | $(-x, y, z)$ |
|---|---|
| $k_x$ | -$k_x$ |
| $k_y$ | $k_y$ |
| $k_z$ | $k_z$ |
| $\sigma_x$ | $\sigma_x$ |
| $\sigma_y$ | -$\sigma_y$ |
| $\sigma_z$ | -$\sigma_z$ |

$$H_{SOI} = \alpha_1 k_x \sigma_z + \alpha_2 k_x \sigma_y + \alpha_3 k_y \sigma_x \tag{4.5}$$

where $k_x$ and $k_y$ are the wave vectors in the $x$ and $y$ directions, respectively, $\sigma_x$, $\sigma_y$, and $\sigma_z$ are Pauli matrixes, and $\alpha_1$, $\alpha_2$, and $\alpha_3$ are coupling constants called as the spin-orbit strength. In this expression, $\alpha_1$ is characterized by the in-plane electric field $E_y$ generated by the in-plane electric polarization $\Delta P_y$, which is induced by the polarity of the present system. On the other hand, $\alpha_2$ and $\alpha_3$ are characterized by the out-of-plane electric field $E_z$, which originates from the out-of-plane electric polarization $\Delta P_z$ induced by the surface effect [see Figure 4.6].

In the case of a bulk system oriented on the $[10\bar{1}0]$ direction, the out-of-plane electric field $E_z$ vanishes. Consequently, in the $k_x - k_y$ plane, both $\alpha_2$ and $\alpha_3$ are zero. This leads to a case in which only the first term in the $H_{SOI}$ equation remains. To confirmed this, we performed fully relativistic calculation of the bulk system oriented on the $[10\bar{1}0]$ direction [Figure 4.7 (a)]. Here, we calculate the band structures along $X - \Gamma - Y$ direction [Figure 4.7 (b)]. We find that that the band splitting is observed in the $\Gamma$-$X$ direction, but it is degenerated in the $\Gamma$-$Y$ direction [Fig. 4.7(c)]. We also performed the spin textures calculation of the spin-split bands and find that the spin textures show fully out-of-plane spin orientation in the $z$ direction [Fig. 4.8]. These calculated results of the band splitting and the spin textures are consistent with the simplified Hamiltonian.

In surface states, on the other hand, a band split is introduced in the $\overline{\Gamma}$-$\overline{Y}$ direction due to the third term in $H_{SOI}$ equation [Fig. 4.3]. Furthermore, as a result of the second term in this equation, a tilting of the spin textures in the in-plane $y$ direction is induced [Fig. 4.4]. It can therefore be concluded that the above

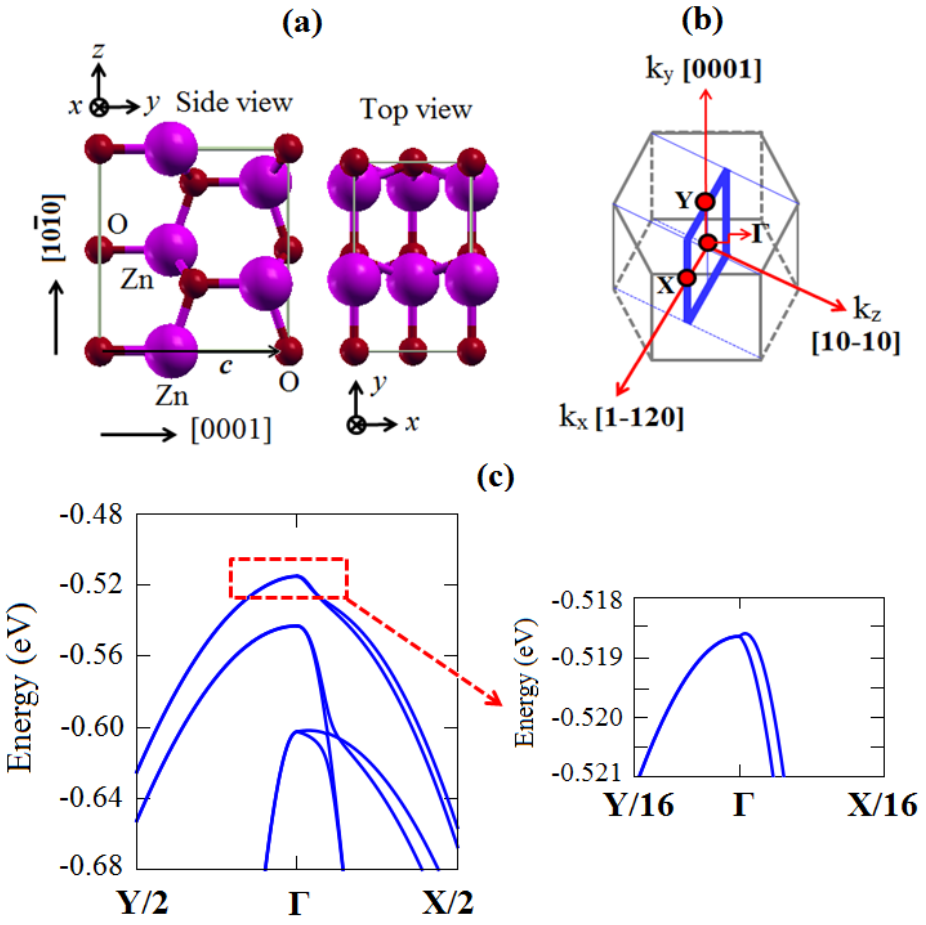


FIGURE 4.7: (a) Crystal structure (top and side views) of the bulk system oriented on the [10$\bar{1}$0] direction. (b) Brillouin zone of the bulk system oriented on the [10$\bar{1}$0] direction. (c) The spin-split band at the valence band maximum (VBM) in the case of bulk system. The insert shows the band splitting of the highest VBM.

spin-orbit Hamiltonian of the surface state also matches well with the calculated results, i.e., the band split in the $\overline{\Gamma}$-$\overline{Y}$ direction and the tilt of the spin textures.

#### 4.3.2.3 Electric polarization analyses

Since $H_{SOI}$ is strongly affected by the electric field as mentioned above, the origin of the spin textures can be further clarified by studying the electric polarization [94]. On the basis that the spin-split surface state is strongly localized in the first two-bilayers [Fig. 4.5], the strong electric polarization is expected to occure in these bilayer. To clarify this, the layer-dependence of the electric polarization was calculated using a point charge model (PCM) for $Zn^{2+}$ and $O^{2-}$ ions in the bilayers to evaluate the polarization difference:

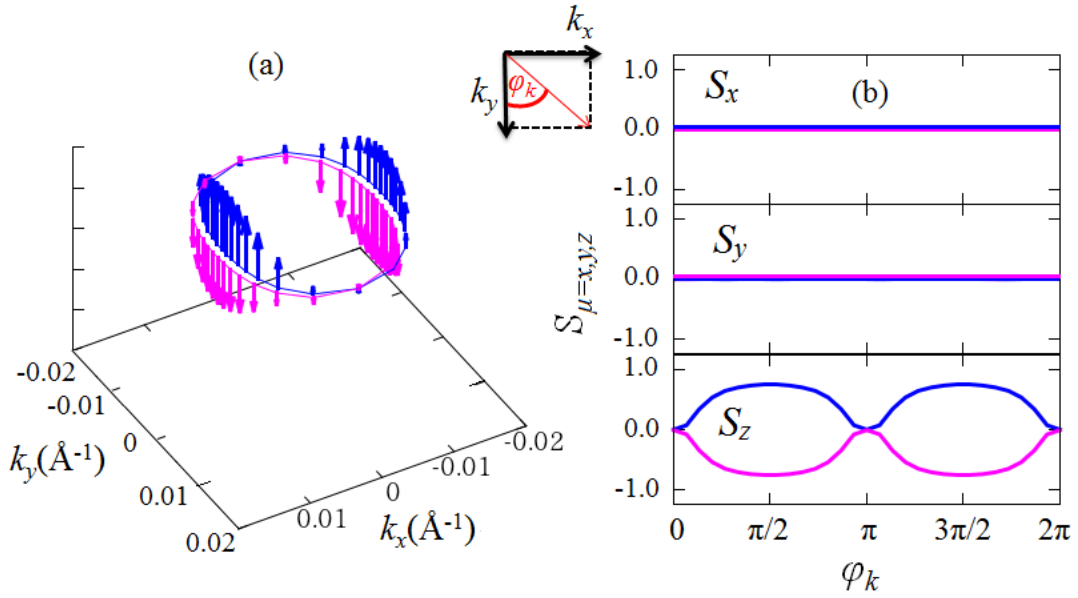


FIGURE 4.8: (a) Spin textures of the the spin-split band at the valence band top in the case of bulk system. (b) Relationships between rotation angle ($\varphi_k$) and spin components.

$$\Delta\mathbf{P} = \mathbf{P}(c/a, u) - \mathbf{P}(c/a, u_{ideal}). \tag{4.6}$$

Here, $c/a$ and $u$ are the lattice constant ratio and internal parameter for a given optimized structure, respectively, and $u_{ideal} = 0.375$. As shown in Fig. 4.9(a), this reveals that the strongest electric polarization is identified near the first bilayer.

TABLE 4.3: The calculated value of the band gap and energy position of the Zn-$d$ orbitals compared with those of previous calculation and experimental results.

| Parameter | surface system | bulk system |
|---|---|---|
| $\Delta P_y$ (C/m$^2$) | -0.081 | -0.027 |
| $\Delta P_z$ (C/m$^2$) | 0.077 | - |

Electric polarization in the out-of-plane $\Delta P_z$ and in-plane $\Delta P_y$ directions was calculated to be 0.077 C/m$^2$ and -0.081 C/m$^2$, respectively [see table 4.3]. These values indicate that the electric field in the out-of-plane $E_z$ direction is comparable to that in the in-plane $E_y$ direction, which would induce a tilting of the spin orientation [Fig. 4.9(b)]. However, only the in-plane electric polarization is observed in the case of bulk system [$\Delta P_{y-\mathtt{bulk}} = -0.0271$ C/m$^2$]. This leads to the fact that the in-plane elctric field $E_y$ is generated, but induces a spin orientation

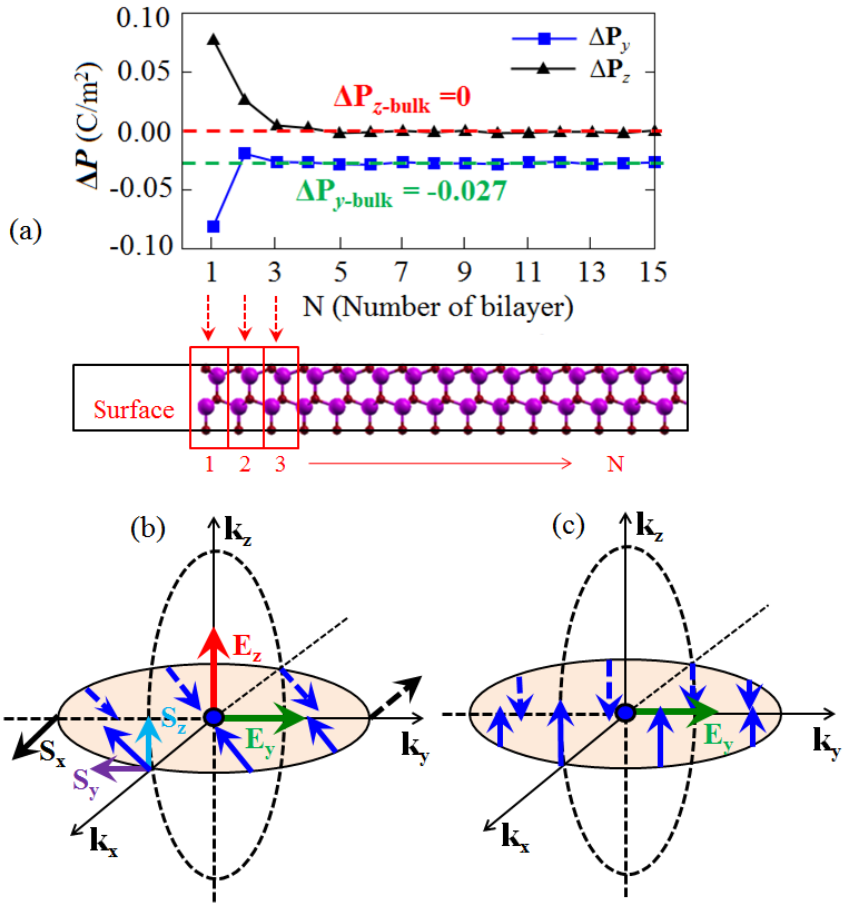


FIGURE 4.9: (a) Calculated data of the in-plane and out-of-plane electric polarizations ( $\Delta P_y$, $\Delta P_z$ ) in each bilayers. The electric polarizations are calculated by using the PCM. Schematic view of the spin textures and electric fields for the case of the surface (c) and bulk systems (d).

with a fully out-of-plane z-direction [Fig. 4.9(c)]. This would confirm that the spin textures in Fig. 4.4 are consistent with the PCM results.

#### 4.3.2.4 Discussion

Recently, PSH that induces a greatly enhanced spin relaxation time has been extensively studied [32–39], with our calculations indicating that this is in fact achieved using the ZnO $(10\bar{1}0)$ surface. Since the spin textures in the calculated results show a quasi-one-dimensional orientation, a magnetic field is induced in a direction parallel to spin orientation. This inhibits the precession of the spins, thereby increasing the spin relaxation time. A similar mechanism behind long

spin relaxation times has been reported in [110]-oriented zinc-blende QWs [109–111], suggesting that the ZnO $(10\bar{1}0)$ surface could provide an efficient spintronics device.

TABLE 4.4: Calculated result of the spin-orbit strenght ($\alpha_{PSH}$) and wave length ($\lambda_{PSH}$) of PSH compared with various zinc-blende quantum well structures.

| Parameters | This work | GaAs/AlGaAs QWs | InAlAs/InGaAs QWs |
|---|---|---|---|
| $\alpha_{PSH}$ (meVÅ) | 34.78 | (3.5 to 4.9) [34], 2.77 [38] | 1.0 [36], 2.0 [37] |
| $\lambda_{PSH}$ ($\mu$m) | 0.19 | (7.3 to 10) [34], 5.5 [38] | - |

For the spintronics devices applications, calculation of the spin-orbit strength $\alpha_{PSH}$ and wavelength $\lambda_{PSH}$ of the PSH is cruscially important. Since our calculated result of the spin-split surfaces states bands and the spin textures shows the PSH states in the $\overline{\Gamma}$-$\overline{X}$ direction, calculation of $\alpha_{PSH}$ and $\lambda_{PSH}$ can be performed by using the band dispersion in this direction. The schematic view of the parabolic band splitting and the shifting Fermi surface is shown in Figure 4.10. The calculation of the spin-orbit strength $\alpha_{PSH}$ can be carried out by evaluation the properties of the band dispersion of the PSH [Fig. 4.10(a)], whereas the wavelength $\lambda_{PSH}$ can be calculated by using the shifting momentum $\mathbf{Q}$ of the two identical Fermi surfaces [Fig. 4.10(b)].

From the properties of parabolic band dispersion [Fig. 4.10(a)], the values of $\alpha_{PSH}$ can be evaluated directly by using the relation

$$\alpha_{PSH} = \frac{2E_R}{k_{0x}} \tag{4.7}$$

where $k_{0x}$ is the momentum off-set in the $\overline{\Gamma}$-$\overline{X}$ direction and $E_R$ is the energy band extremum with respect to the energy for which the band cross at $k_x = 0$ in the $\overline{\Gamma}$-$\overline{X}$ direction.

Subsequently, the wavelength of the PSH $\lambda_{PSH}$ can be calculated by using the relation,

$$\lambda_{PSH} = \frac{2\pi}{Q} \tag{4.8}$$

where $Q$ is the magnitude values of the shifting wave vector $\mathbf{Q}$ in the Fermi surfaces [Fig. 4.10(b)].

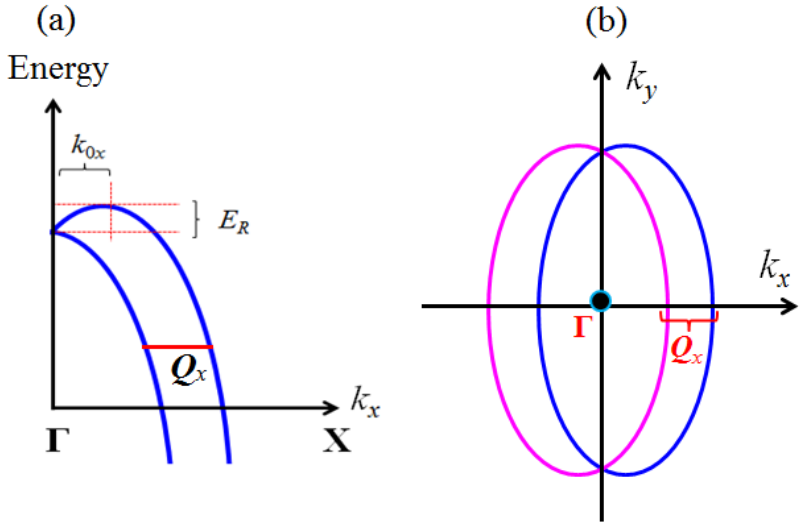


FIGURE 4.10: (a) Schematic view of the band dispersion along $\overline{\Gamma}$-$\overline{X}$ direction. The spin-orbit strength of the PSH can be evaluated directly from this band dispersion. (b) Shifting of the two identical Fermi surfaces by the wave vector **Q**. The wavelenght of the PSH is inversely proportional to the wave vector **Q**.

Tabel 4.4 shows the calculated result of the $\alpha_{PSH}$ and $\lambda_{PSH}$. We found that the value of $\alpha_{PSH}$ is quite substantial (34.78 meVÅ) and much larger than what has been observed in the PSH of various zinc-blende n-type QW structures of GaAs/AlGaAs [(3.5 to 4.9 meVÅ) [34], (2.77 meVÅ) [38]] and InAlAs/InGaAs [(1.0 meVÅ) [36], (2.0 meVÅ) [37]]. This large value of $\alpha_{PSH}$ should ensure a small wavelength of PSH ($\lambda_{PSH}$), which is important to the miniaturization of spintronics devices. As it happens, the calculated value $\lambda_{PSH}$ (0.19 $\mu$m) was in fact one-order less than that observed in the direct mapping of PSH (7.3 to 10 $\mu$m) [34] and the resonant inelastic light-scattering measurement (5.5 $\mu$m) [38] of GaAs/AlGaAs QWs.

## 4.4 Conclussion

We have systematically studied the effect of SOI on a ZnO $(10\overline{1}0)$ surface through first-principles DFT calculations. Here, we in the first time found that the SOI leads to the novel system called as persisten spin helix (PSH), exhibiting a quasi-one-dimensional orientation of the spin textures. Our finding of the PSH is expected to induce the strongly enhanced the spin relaxation time, which is important to realize energy-saving spintronics devices. Furthermore, we revealed that

the wavelength of this PSH is smaller than that observed on various zinc-blende quantum well structures, suggesting that the present system enables for the miniaturization of the spintronics devices.

In our study, we found that that PSH can be achieved by using a wurtzite ZnO $(10\bar{1}0)$ surface with in-plane electric polarization and mirror symmetry. We emphasized that the approach used the present calculations is not limited only for ZnO wurtzite surfaces, but also can be generalized to a variety of SOI system with in-plane electric polarization and mirror symmetry. Here, a special attention was given to the other wurtzite system materials such as GaN and InN, where it is expected that a similar PSH should be observed.

Finally, we concluded that the present system is suitable for future spintronics devices applications.

# Chapter 5

# Summary

## 5.1 Conclussion

In this dissertation, the effect of SOI on the wurtzite ZnO has been studied by using fully-relativistic DFT calculations. We investigate the spin textures to identify the new physical properties induced by the SOI. Here, two different systems has been studied, (i) the strained bulk system, and (ii) the surface system oriented on the $[10\bar{1}0]$ direction. In the following sections, we present the conclusion for these two topics.

### 5.1.1 Rashba effect on strained ZnO

In the first study, we have investigated the effect of SOI on the strained bulk ZnO by using first-principles DFT calculations. We found that strain controls the SOI in ZnO, where the inversion Rashba spin rotations are observed between tensile and compressive biaxial strain. We also found that the Rashba spin-orbit strength can be effectively controlled by tuning the strain. Our finding of the inversion Rashba rotation may give some hint for the application of the future spintronisc devices.

According to our finding, the presently used calculation scheme is expected to be useful tools to investigate the Rashba effect on the SOI system materials. Here, a special attention is given to the system having large internal electric field such as oxide interface system materials. Recently, the interface system such as

MgZnO/ZnO were extensively studied [54]. Our study clarified that the effect of strain on interfaces plays an important role in SOI.

### 5.1.2 Persistent spin helix on ZnO $(10\bar{1}0)$ surface

In the second study, we have investigated the effect of SOI on ZnO $(10\bar{1}0)$ surface. Here, we in the first time found that the SOI leads to the novel system called as persisten spin helix (PSH), exhibiting a quasi-one-dimensional orientation of the spin textures. Our finding of the PSH is expected to induce the strongly enhanced the spin relaxation time, which is important to realize energy-saving spintronics devices. Furthermore, we revealed that the wavelength of this PSH is smaller than that observed on various zinc-blende quantum well structures, suggesting that the peresent system enables for the miniaturization of the spintronics devices.

In the present study, we found that that PSH can be induced by using a surface system with in-plane electric polarization and mirror symmetry. We emphasized that this approach is not only limited for ZnO wurtzite surfaces, but also can be generalized to a variety of SOI system materials with in-plane electric polarization and mirror symmetry. Here, a special attention is given to the other wurtzite system materials such as GaN and InN, where it is expected that a similar PSH should be observed.

Finally, we concluded that the present system is suitable for future spintronics devices applications.

## 5.2 Future direction

The new physical properties induced by the SOI have been found in the strained bulk and surface systems of wurtzite ZnO. However, it should be noted that both systems have insulating phase. Recently, the new phases of ZnO $(10\bar{1}0)$ surface has been reported exhibiting the metallic phase, which is achieved at room temperature by using hydrogen adsorption [112, 113]. Experimental observation of metallicity on the hydrogeneted ZnO $(10\bar{1}0)$ surface opens the new possibility to explore the SOI on the metallic surface state, which is expected to induce new useful properties for spintronics.

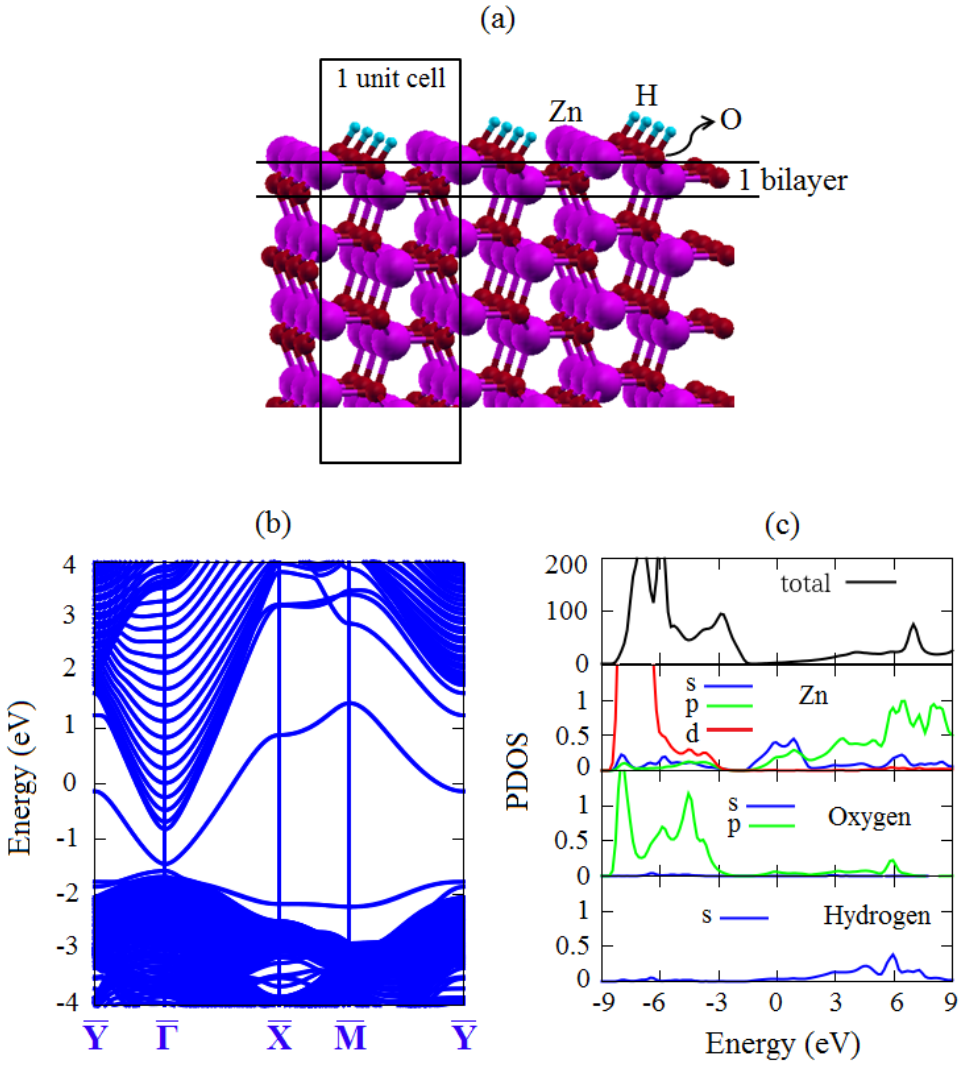


FIGURE 5.1: (a) Crystal structure of hydrogeneted ZnO ($10\bar{1}0$ surface. (b) band structure of hydrogeneted ZnO ($10\bar{1}0$) surface. (c) Density of states projected to the surface atoms.

We have performed preliminary calculations on the hydrogeneted ZnO ($10\bar{1}0$) surface [Figure 5.1(a)] using first-principles DFT calculations. As shown in Figure 5.1 (b), we revealed that the metallicity appear in the band structures, which is consistent with the past experiment[112, 113]. By using the same calculation scheme used in the present study, it is expected that the new physical properties induced by SOI can be observed on the metallic surface states.

# Bibliography

[1] I. Zutic, J. Fabian, and S. D. Sarma, Rev. Mod. Phys. 76, 323 (2004).

[2] A. Hirohata and K. Takanashi, J. Ohys. D: Apl. Phys. 47, 193001 (2014).

[3] W. Pauli, Z. Physik 31, 765 (1925).

[4] W. Gerlach and O. Stern, Z. Phys. 9, 349 (1922).

[5] W. Gerlach and O. Stern, Z. Phys. 9, 353 (1922).

[6] F. Bitter, Phys. Rev. 41, 507 (1932).

[7] G. Prinz, Science 282, 1660 (1998).

[8] S. A. Wolf et. al., Science 294, 1488 (2001).

[9] M. N. Baibich et. al., Phys. Rev. Lett. 61, 2472 (1988).

[10] G. Binasch et. al., Phys. Rev. B 39, 4828 (1989).

[11] M. Julliere, Phys. Lett. A 54, 225 (1975).

[12] S. Maekawa and U. Gafvert, IEEE Trans. Magn. 18, 707 (1982).

[13] T. Miyazaki and N. Tezuka, J. Magn. Magn. Mater. 139, L231 (1995).

[14] J. S. Moodera et. al., Phys. Rev. Lett. 74, 3273 (1995).

[15] J. S. Moodera and J. Mathon, J. Magn. Magn. Mater. 200, 248 (1999).

[16] R. Fiederling et. al., Nature 402, 787 (1999).

[17] H. Ohno et. al., Nature 408, 944 (2000).

[18] H. Ohno et. al., Nature 790, 944 (1999).

[19] M. Tanaka and Y. Higo, Phys. Rev. Lett. 87, 026602 (2001).

[20] S. Mishra, G. S. Tripathi, and S. Satpathi, Phys. Rev. B 77, 125216 (2008).

[21] J. Bao et. al., Nature 2, 175 (2003).

[22] A. Oiwa et. al., Phys. Rev. Lett. 88, 137202 (2002).

[23] A. Gupta et. al., Science 292, 2458 (2001).

[24] D. Awschalom and N. Samirth, Physics 2, 50 (2009).

[25] Y. A. Bychkov and E. I. Rashba: J. Phys. C 17 (1984) 6039.

[26] E. A. de Andrada e Silva, G. C. La Roca, and F. Bassani, Phys. Rev. B 50, 8523 (1994).

[27] J. Nitta, T. Akazaki, H. Takayanagi, and T. Enoki, Phys. Rev. Lett. 78, 1335 (1997).

[28] G. Dresselhauss, Phys. Rev. 100, 580 (1955).

[29] S. Datta and B. Das: Appl. Phys. Lett. 56 (1990) 665-667.

[30] S. Kuhlen, K. Schmalbuch, M. Hagedorn, P. Schlammes, M. Patt, M. Lepsa, G. Guntherodt, and B. Beschoten, Phys. Rev. Lett. 109, 146603 (2012).

[31] X.-L. Qi, Y.-S. Wu, and S.-C. Zhang, Phys. Rev. B 74, 085308 (2006).

[32] B. A. Bernevig, J. Orenstein, and S.-C. Zhang, Phys. Rev. Lett. 97, 236601 (2006).

[33] J. D. Koralek, C. P. Weber, J. Orenstein, B. A. Bernevig, S.-C. Zhang, S. Mack, and D. D. Awschalom, Nature 458, 610 (2009).

[34] M. P. Walser, C. Reichl, W. Wegscheider, and G. Salis, Nat. Phys. 8, 757 (2012).

[35] M. Kohda, V. Lechner, Y. Kunihashi, T. Dollinger, P. Olbrich, C. Schonhuber, I. Caspers, V. V. Bel'kov, L. E. Golub, D. Weiss, K. Richter, J. Nitta, and S. D. Ganichev, Phys. Rev. B 86, 081306 (2012).

[36] J. Ishihara, Y. Ohno, and H. Ohno, Applied Physics Express 7, 013001 (2014).

[37] A. Sasaki, S. Nonaka, Y. Kunihashi, M. Kohda, T. Bauernfeind, T. Dollinger, K. Richter, and J. Nitta, Nat. Nano. 9, 703 (2014).

[38] C. Schonhuber, M. P. Walser, G. Salis, C. Reichl, W. Wegscheider, T. Korn, and C. Schuller, Phys. Rev. B 89, 085406 (2014).

[39] Y. S. Chen, S. Falt, W. Wegscheider, and G. Salis, Phys. Rev. B 90, 121304 (2014).

[40] Y. K. Kato, R. C. Myers, A. C. Gossard, and D. D. Awschalom, Nature 427, 50 (2004).

[41] R. Dingle et. al., Appl. Phys. Lett. 33, 665 (1978).

[42] V. Umansky, R. de-Picciotto, and M. Heblum, Appl. Phys. Lett. 71, 683 (1997).

[43] P. Diez et. al., Appl. Phys. Lett. 88, 052107 (2006).

[44] B. R. K. Nanda and S. Satpathi, Phys. Rev. Lett. 101, 127201 (2008).

[45] P. Mutakef et. al., App. Phys. Lett. 99, 232116 (2011).

[46] Y. Wang et. al., Phys. Rev. B 79, 212408 (2009).

[47] J. D. Burton and E. Y. Tsymbal, Phys. Rev. Lett. 107, 166601 (2011).

[48] L. Schmidt-Mende and J. L. MacManus-Driscoll, Mater. Today 10, 40 (2007).

[49] A. Tsukazaki, A. Ohtomo, T. Kita, Y. Ohno, H. Ohno, and M. Kawasaki, Science 315, 1388 (2007).

[50] A. Tsukazaki, S. Akasaka, K. Nakahara, Y. Ohno, H. Ohno, D. Maryenko, A. Ohtomo, and M. Kawasaki, Nat. Mater. 9, 889 (2010).

[51] J. Ye et. al., Sci. Rep. 2, 533, (2012).

[52] K. Han, N. Tang, J. D. Ye, J. X. Duan, Y. C. Liu, K. L. Teo, and B. Shen, Appl. Phys. Lett. 100, 192105 (2012).

[53] S. Ghosh, V. Sih, W. H. Lau, and D. D. Awschalom, Appl. Phys. Lett. 86, 232507 (2005).

[54] Y. Kozuka, S. Teraoka, J. Falson, A. Oiwa, A. Tsukazaki, S. Tarucha, and M. Kawasaki, Phys. Rev. B 87, 205411 (2013).

[55] S. LaShell, B. A. McDougall, and E. Jeusen, Phys. Rev. Lett. 77, 3419 (1996).

[56] M. Yu et. al., Phys. Rev. Lett. 93, 046403 (2004).

[57] O. Krupin et. al., Phys. Rev. B 71, 201403(R) (2005).

[58] G. Nicolay et. al., Phys. Rev. B 65, 033407 (2001).

[59] M-H. Liu, C-R. Chang, and S-H. Chen, Phys. Rev. B 71, 153305 (2005).

[60] M. I. D'yakonov and V. I. Perel', Sov. Phys. Solid State 13, 3023 (1972).

[61] D. R. Hartree, Proc. R. Soc. London A13, 621 (1928).

[62] V. Fock, Z. Phys. 61, 126 (1930).

[63] J. C. Slater, Phys. Rev. 81, 385 (1951).

[64] P. Hohenberg and W. Kohn, Phys. Rev. 136, 864, (1964).

[65] W. Kohn and L. J. Sham, Phys. Rev. 140, 1133 (1965).

[66] J. P. Perdew, K. Burke, and M. Ernzerhof, Phys. Rev. Lett. 77, 3865 (1996).

[67] T. Ozaki, H. Kino, J. Yu, M. J. Han, N. Kobayashi, M. Ohfuti, F. Ishii, T. Ohwaki, H. Weng, M. Toyoda, and K. Terakura: http://www.openmx-square.org/

[68] N. Troullier and J. L. Martins, Phys. Rev. B 43, 1993 (1991).

[69] T. Ozaki, Phys. Rev. B 67, 155108 (2003).

[70] T Ozaki, and H. Kino, Phys. Rev. B 69, 19511 (2004).

[71] J. J. Sakurai, Modern Quantum Mechanics.

[72] U. Von barth and L. Hedin, J. Phys. C 5, 1629 (1972).

[73] J. Kubler, K-H. Hock, J. Sticht, and A. R. William, J. Phys. F 18, 469 (1988).

[74] H. Kotaka, F. Ishii, and M. Saito, Jpn. J. Appl. Phys. 52, 035204 (2013).

[75] P. V. Rysselberghe, J. Phys. Chem. 36, 1152 (1932).

[76] R. D. King-Smith and D. Vanderbilt, Phys. Rev. B 47, 1651 (1993).

[77] R. Resta, Rev. Mod. Phys. 66, 889 (1994).

[78] Y. Wu, G. Chen, S.-H. Wei, M. Al-Jassim, and Y. Yan, Phys. Rev. B 86, 155205 (2012).

[79] T. Koga, J. Nitta, and H. Takayanagi, Phys. Rev. Lett. 88, 126601 (2002).

[80] F. Oba, A. Togo, I. Tanaka, J. Paier, and G. Kresse, Phys. Rev. B 77, 245202 (2008).

[81] R. Girrard, O. Tjernberg, G. Chiaia, S. Sderholm, U. karlsson, C. Wigren, H. Nyln, and I. Lindau, Surf. Sci. 373, 409 (1997).

[82] U. Ozgur, Y. Alivov, C. Liu, A. Teke, M. Reshchikov, S. Dogan, V. Avrutin, S. Cho, and H. Morkoc, J. Appl. Phys. 98, 041301 (2005).

[83] J. Heyd, G. E. Scuseria, and M. Ernzerhof, J. Chem. Phys. 118, 8207 (2003).

[84] L. Weston, X. Y. Cui, B. Delley, and C. Stampfl: Phys. Rev. B 86 (2012) 205322.

[85] A. Janotti and C. G. Van de Walle, Phys. Rev. B 76, 165202 (2007).

[86] A. Zoroddu, F. Bernardini, P. Ruggerone, and V. Fiorentini, Phys. Rev. B 64, 045208 (2001).

[87] R. Dutta and N. Mandal, Appl. Phys. Lett. 101, 042106 (2012).

[88] A. Malashevich and D. Vanderbilt, Phys. Rev. B 75, 045106 (2007).

[89] A. D. Corso, M. Posternak, R. Resta, and A. Baldareschi, Phys. Rev. B 50, 10715 (1994).

[90] H. Matsui and H. Tabata, J. Appl. Phys. 113, 183525 (2013).

[91] R. Ghosh, D. Basak, and S. Fujihara, J. Appl. Phys. 96, 2689 (2004) .

[92] P. pant, J. D. Budai, and J. Narayan, Acta Mater. 58, 1097 (2010).

[93] M. Al-suleiman et al., Appl. Phys. Lett. 91, 081977 (2007).

[94] M. A. U. Absor, H. Kotaka, F. Ishii, and M. Saito., Appl. Phys. Express. 7, 053002 (2014).

[95] T. Koga, J. Nitta, H. Takayanagi, and S. Datta, Phys. Rev. Lett. 88, 126601 (2002).

[96] P. Foldi, B. Molnar, M. G. Benedict, and F. M. Peeters, Phys. Rev. B 71, 033309 (2005).

[97] A. Tsukazaki, S. Akasaka, K. Nakahara, Y. Ohno, H. Ohno, D. Maryenko, A. Ohtomo, and M. Kawasaki, Nat. Mater. 9, 889 (2010).

[98] O. Ambacher, J. Smart, J. R. Shealy, N. G. Weimann, K. Chu, M. Murphy, W. J. Schaff, L. F. Eastman, R. Dimitrov, L. Wittmer, M. Stutzmann, W. Rieger, and J. Hilsenbeck, Journal of Applied Physics 85 (1999).

[99] C. B. Duke, R. J. Meyer, A. Paton, and P. Mark, Phys. Rev. B 18, 4225 (1978).

[100] B. Meyer and D. Marx, Phys. Rev. B 67, 035403 (2003).

[101] P. Schroer, P. Kruger, and J. Pollmann, Phys. Rev. B 49, 17092 (1994).

[102] N. L. Marana, V. M. Longo, E. Longo, J. B. L. Martins, and J. R. Sambrano, J. Phys. Chem. A 112, 8958 (2008).

[103] H. H. Zhang, X. H. Pan, Y. Li, Z. Z. Ye, B. Lu, W. Chen, J. Y. Huang, P. Ding, S. S. Chen, H. P. He, J. G. Lu, L. X. Chen, and C. L. Ye, Applied Physics Letters 104, 112106 (2014).

[104] P. Ding, X. Pan, J. Huang, H. He, B. Lu, H. Zhang, and Z. Ye, J. Cryst. Growth 331, 15 (2011).

[105] T. Oguchi and T. Shishidou, Journal of Physics: Condensed Matter 21, 092001 (2009).

[106] E. Simon, A. Szilva, B. Ujfalussy, B. Lazarovits, G. Zarand, and L. Szunyogh, Phys. Rev. B 81, 235438 (2010).

[107] S. Vajna, E. Simon, A. Szilva, K. Palotas, B. Ujfalussy, and L. Szunyogh, Phys. Rev. B 85, 075404 (2012).

[108] R. Requist, P. M. Sheverdyaeva, P. Moras, S. K. Mahatha, C. Carbone, and E. Tosatti, Phys. Rev. B 91, 045432 (2015).

[109] S. Dohrmann, D. Hagele, J. Rudolph, M. Bichler, D. Schuh, and M. Oestreich, Phys. Rev. Lett. 93, 147405 (2004).

[110] O. D. D. Couto, F. Iikawa, J. Rudolph, R. Hey, and P. V. Santos, Phys. Rev. Lett. 98, 036603 (2007).

[111] Y. Ohno, R. Terauchi, T. Adachi, F. Matsukura, and H. Ohno, Phys. Rev. Lett. 83, 4196(1999).

[112] K. Ozawa and K. Mase, Phys. Rev. Lett. 83, 125406(2011).

[113] Y. Wang at. al., Phys. Rev. Lett. 95, 266104 (2005).